water

MDPI

Article

Improving Thermal Distribution in Water-Cooled PV Modules and Its Effect on RO Permeate Recovery

Mario F. Suzuki Valenzuela [1], Fernando Sánchez Soto [2], María Magdalena Armendáriz-Ontiveros [2], Ian M. Sosa-Tinoco [1] and Gustavo A. Fimbres Weihs [3,*]

[1] Departamento de Ingeniería Eléctrica y Electrónica, Instituto Tecnológico de Sonora, 5 de Febrero 818 Sur, Cd. Obregón, Sonora C.P. 85000, Mexico; mario.suzuki89094@potros.itson.edu.mx (M.F.S.V.); ian.sosa@itson.edu.mx (I.M.S.-T.)

[2] Departamento de Ciencias del Agua y Medio Ambiente, Instituto Tecnológico de Sonora, 5 de Febrero 818 Sur, Cd. Obregón, Sonora C.P. 85000, Mexico; fersancheziq@gmail.com (F.S.S.); maria.armendariz@itson.edu.mx (M.M.A.-O.)

[3] School of Chemical and Biomolecular Engineering, The University of Sydney, Sydney, NSW 2006, Australia

* Correspondence: gustavo.fimbresweihs@sydney.edu.au; Tel.: +61-2-9351-5284

Abstract: Among the most notable emerging hybrid technologies for water treatment are those that combine reverse osmosis (RO) membrane systems with alternative energy sources such as solar photovoltaic (PV). Solar PV modules can enable systems disconnected from the electricity grid, and in some locations can also be used for water heating as photovoltaic-thermal (PVT) units, a process in which water removes heat from the PV module, increasing its electrical generation efficiency. When combined with RO, the higher temperature feed water can increase RO permeate flux, improving recovery but decreasing the rejection of dissolved salts. Although the decrease in efficiency of PV modules at higher temperatures is a well-known issue, this is usually under conditions of uniform temperature. However, the temperature distribution in water-cooled PV modules is usually not uniform and, given the anisotropy of the distribution and electrical connection of the PV cells in the module, this factor has not been the focus of much study. In this context, a PVT unit that focuses on increasing the output water temperature with a high global heat transfer coefficient will not necessarily be the most electrically efficient system. This study experimentally assesses several proposed heat-exchange configurations for PVT systems where the PV modules are cooled by forced convective water flow. A simulation model of PVT performance is then validated and used to predict the productivity of the PVT-RO coupling, both in terms of electrical generation and permeate flux of the hybrid system under different conditions. The results suggest that water-cooled PV modules have several potential applications for off-grid and remote water treatment, as well as water transportation systems.

Keywords: solar energy; PV modules; reverse osmosis; solar desalination; PVT

Citation: Suzuki Valenzuela, M.F.; Sánchez Soto, F.; Armendáriz-Ontiveros, M.M.; Sosa-Tinoco, I.M.; Fimbres Weihs, G.A. Improving Thermal Distribution in Water-Cooled PV Modules and Its Effect on RO Permeate Recovery. *Water* **2021**, *13*, 229. https://doi.org/10.3390/w13020229

Received: 18 December 2020
Accepted: 15 January 2021
Published: 19 January 2021

1. Introduction

In response to growing concerns about the impact of climate change on vital resources, experts have proposed the concept of a water–energy–food security nexus, which is one of the most accepted ways to understand and approach sustainable development [1]. This concept, first introduced at the 2008 World Economic Forum, states that there is an inherent interconnection between these three sectors (water, energy and food), and therefore the actions taken in one of them can have an effect in one or both other sectors [2]. One of the most promising technologies that fall under this framework is renewable energy-powered reverse osmosis (RO) for water desalination. RO can provide fresh water year-round by using alternative water sources, such as seawater or brackish water, helping mitigate the water scarcity problem [3]. However, energy consumption is the main cost driver for RO, representing 44% of operating costs. Large energy requirements coupled with high energy prices raise the cost of RO product water [4], making this process economically unfeasible for many low-income regions.

To reduce the problem of high RO costs, much research has focused on coupling RO desalination plants to different types of renewable energy, such as solar photovoltaic (PV), wind, ocean wave power or hybrid systems [5,6]. Since arid regions experiencing water stress are commonly located in dry climate regions that present high levels of solar irradiation, solar power generation seems a logical technology for this application. Accordingly, solar PV is the most commonly used renewable energy for RO, mainly due to the technical and economic advantages of its installation [7]. For example, Rezk et al. [8] operated a 150 m^3 d^{-1} RO desalination plant powered by solar PV and self-charging fuel cells. They found a 70% cost reduction in comparison with a diesel generation system. Elmaadawy et al. [9] designed a renewable energy system to operate a seawater RO desalination plant powered by photovoltaic-wind-diesel energy and found a 61% net present cost reduction. Mostafaeipour et al. [10] tested and proposed a novel brackish water RO desalination system powered by photovoltaic energy, and found a 21% product water cost reduction. Hence, given recent capital cost reductions for renewable energy and the ability to operate RO systems when energy is available, powering RO desalination plants with renewable energy is likely to decrease operating costs significantly, producing low-cost water for human usage with near-zero emissions.

Although solar PV modules can transform radiant energy from the sun into electricity, their efficiency is relatively low (usually less than 20%), and it decreases with increasing temperature [11]. As a "rule of thumb", it has been estimated that a solar PV module loses 0.5% of efficiency for each 1 °C increase in temperature [12,13]. Research has been conducted to identify other conditions that may also reduce the efficiency of PV modules, such as non-uniform illumination [14,15] and non-uniform temperature distribution over the module surface, which causes current mismatch and could lead to permanent structural damage due to thermal tensions [16].

Many researchers have obtained positive results by implementing passive and active cooling technologies on PV modules. Siecker et al. [13] provide a comparison between different cooling methods (both active and passive) in terms of minimising the effects of increasing temperature, while trying to improve the performance of PV modules. Active cooling methods usually refer to forced convection, where a cooling fluid is driven by a pump or blower which requires additional energy to operate. On the other hand, passive cooling refers to natural convection, where the flow of cooling fluid is driven by density gradients caused by a temperature difference, so they do not require additional energy to operate. A hybrid solar photovoltaic–thermal (PVT) module cooled by forced water circulation is a common example of active cooling, in which water enters and exits the module at defined locations. These systems have the dual objective of electricity production and water heating. The positions of the inlets and outlets influence the fluid flow inside the heat exchanger, and this is commonly controlled by fixing the flow channels in the heat exchanger design [13,17].

Research shows that the overall energy (thermal + electrical) efficiency of a PV module can be increased to 40% if it is cooled in a PVT arrangement [18]. For PV-RO coupling purposes, the PVT system stands out as one of the best options. It usually consists of a heat exchanger mounted on the back of the PV module, through which a cooling fluid is circulated, removing heat from the silicon cells of the PV module and increasing their electrical generation. This is convenient for PV-RO coupling for two reasons: (a) the RO feed water (e.g., seawater or brackish water) can be used as the circulating fluid, increasing its temperature; (b) the higher temperature feed water can increase RO permeate flux, improving recovery, and therefore generating more product water for a given membrane area, albeit decreasing the rejection of dissolved salts [19]. At the time of writing, there is only one study reporting a RO desalination plant operated with PVT cooling, finding an increased efficiency for PVT due to cooling and fewer required modules [20].

Although the decrease in the efficiency of PV modules at higher temperatures is a well-known issue, this has traditionally been investigated under conditions of uniform temperature. However, temperature distribution in water-cooled PV modules is usually not uniform [16] and, given the anisotropy of the distribution and electrical connection of the PV cells in the module, this factor has not been the focus of much study and is not well understood. In this context, a PVT unit that focuses on increasing the output water temperature with a high global heat transfer coefficient will not necessarily be the most electrically efficient system. Given that important efforts are currently underway to power RO desalination plants with renewable energy, and that increasing the solar energy efficiency of PVT modules is desirable, this study experimentally assesses several proposed heat-exchange configurations for PVT systems where the PV modules are actively cooled by forced convective water flow. Emphasis is made on understanding the flow characteristics that lead to better temperature distribution and larger efficiency gains compared to modules without active cooling. A simulation model of PVT performance is then validated and used to predict the productivity of the PVT-RO coupling, both in terms of electrical generation and permeate flux of the hybrid system under different conditions. The RO simulation assumes a 1D non-isothermal model which calculates the variation in water properties (i.e., density and viscosity based on concentration, pressure, and temperature) along with the membrane permeance at different operating temperatures to predict permeate production. Hence, this paper presents the first study of a RO desalination system operated with PVT cooling which considers the effect of varying temperature at the RO feed. The insights gained are applicable for environmental conditions with high solar irradiation, high ambient temperature and low humidity, such as those in northwest Mexico.

2. Materials and Methods

A PVT module was designed and constructed, incorporating 16 fluid inlets/outlets at distinct locations on the back of the PV module (functioning as a heat exchanger), which are used for cooling via forced convection with water as the cooling fluid. Forced convection (as opposed to natural convection) is selected as the cooling strategy because RO systems already require a pumping system for their operation, so implementing this strategy does not require additional pumping equipment. Nonetheless, forced convection does involve an increase in pressure losses within the heat exchanger on the back of the PV module, which in turn requires more pumping energy. There is therefore a trade-off when implementing forced convection as the active cooling method, i.e., between the additional energy generated from the PV efficiency increase and the additional energy consumption due to pressure losses.

Experimental data is collected by measuring the electrical and thermal performance of the PVT module under two different flow rates (1 and 2 L min^{-1}) and 11 different inlet/outlet heat exchange configurations as described in Appendix A. The collected data is used to validate a numerical model, which is then used to predict the daily water production of a PVT-RO plant under different combinations of flow rate and heat exchange configuration, for distinct weather conditions. Detailed explanations of the experimental and numerical methods employed are described in the following sections.

2.1. Characterisation of the PV Module

Commercial PV modules (AXITEC AC-270-P polycrystalline cells) were used for the experimental tests. Table 1 shows the technical specifications for these modules, according to the manufacturer, at standard test conditions (1000 W m^{-2} solar irradiation and 25 °C).

Table 1. Electrical generation properties for the AXITEC AC-270-P modules at standard test conditions.

Parameter	Value	Units
Rated power	270	W
Rated voltage	31.12	V
Rated current	8.71	A
Short circuit current (I_{cc})	9.25	A
Open circuit voltage (V_{oc})	38.21	V
Efficiency (η)	16.60	%
Fill factor (F_F)	0.766	-
Dimensions	$1640 \times 992 \times 35$	mm
Effective area (A_{PV})	1.47	m^2
Operating temperature	-40 to 85	°C

The configuration of the PV cells in the module is distributed in 3 groups of 20 cells connected in series. Each group is formed by two columns of 10 cells in series, and the groups are connected in series with each other by means of diodes. This forms a rectangular arrangement of 6×10 cells in the panel, as shown in Figure 1. The arrangement of the PV cells is a characteristic that impacts how cooling may affect any efficiency increases, this due to the dependence of electricity generation between the groups. The group with the cell or cells with highest resistance (due to a higher temperature) may activate the bypass diode and will limit the amount of energy produced by the array. Hence, if there is a large temperature gradient, it should theoretically affect the least number of groups if it is aligned with the groups (i.e., in the horizontal direction).

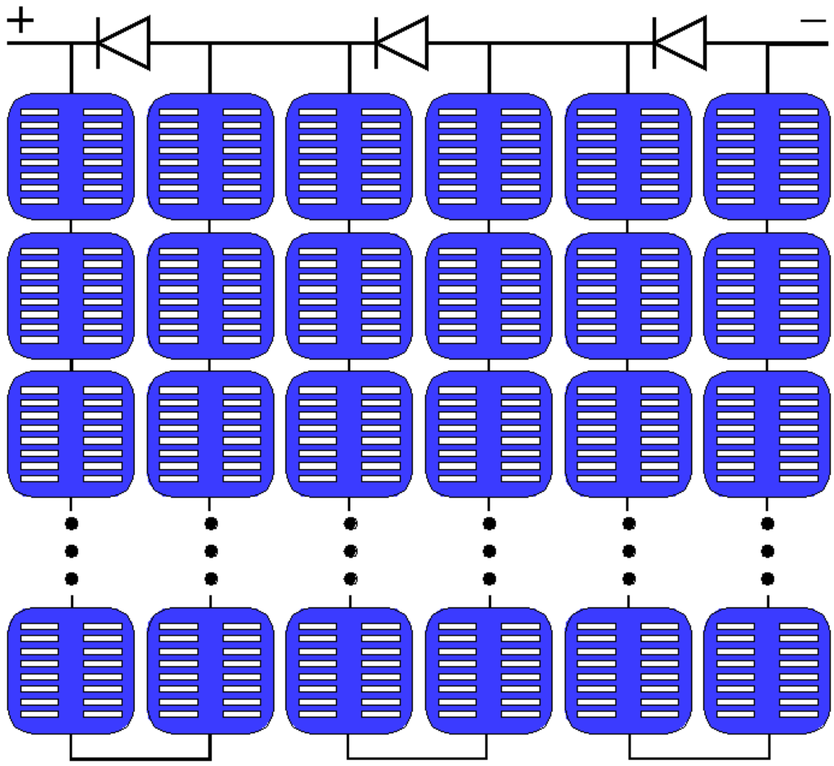

Figure 1. Arrangement of PV cells in PV module.

The solar modules are electrically characterised by running a power output test under different electric charging conditions, through the capacitor charging method for an I–V curve tracer [21], as depicted in Figure 2.

This test consists of connecting the PV module to a large capacitor C with a Switch (SW_1) and to two sensor probes (A, V), both connected to an oscilloscope. The capacitor is then discharged through a large resistor R by activating SW_2 and disconnecting SW_1. This cycle is repeated several times for statistical analysis. The data collected from this test are then used to trace the characteristic I-V curve for the PV module. This characterisation was conducted at a solar irradiation value of 1000 W m^{-2} and an average module temperature of 59.2 °C.

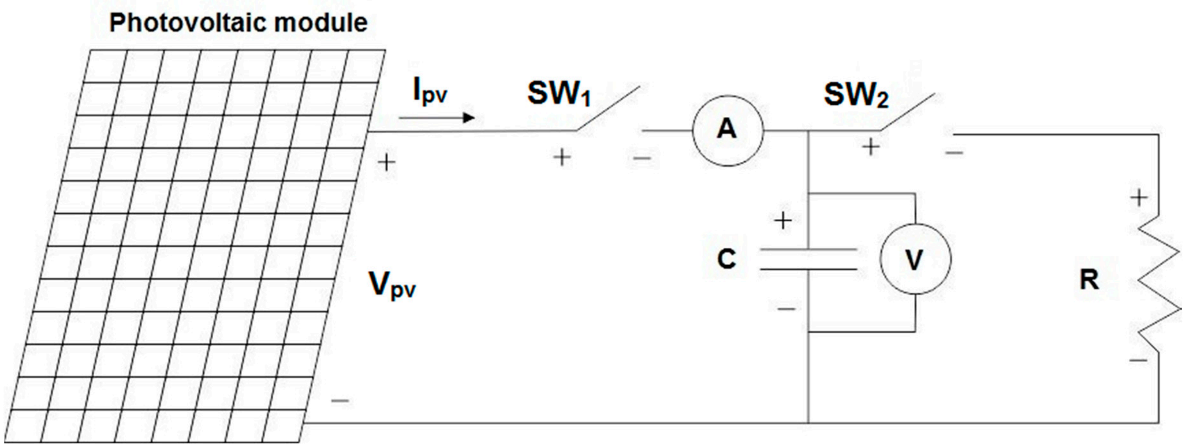

Figure 2. PV Module I-V curve extraction circuit. I_{pv}: PV module current, V_{pv}: PV Module voltage, SW_1: Load capacitor switch 1, SW_2: Load resistor switch 2, A: Oscilloscope Current sensing probe, V: Oscilloscope voltage sensing probe, C: Capacitor load, R: Resistor load.

The relationship between the electrical efficiency of the module and its operating temperature is determined experimentally at a uniform temperature and constant solar irradiation. This is achieved by cooling the PV module using ice, distributed over the surface of the panel. The temperature is monitored until it reaches 10 °C; then, the ice and excess moisture are removed, and finally the open circuit voltage and short circuit current of the PV panel are measured. The measurements are continued while the temperature of the panel increases due to the warm ambient conditions, with data collected in triplicate each time an increment of 5 °C is detected.

The electrical efficiency of the PV module is calculated using the Fill Factor (*FF*), which is the ratio of maximum obtainable power to the product of open circuit voltage and short circuit current. The calculation of the efficiency (η) considers the energy produced with respect to the received solar energy. For this work, the efficiency is determined by:

$$\eta = \frac{V_{oc} I_{sc} FF}{G_s A_{PV}} \quad (1)$$

where G_s is the solar irradiation, V_{oc} is the open-circuit voltage, I_{sc} is the short circuit current, and A_{PV} is the active area of the PV module.

2.2. PVT Module Design

A heat exchanger is adapted into the PV module, consisting of a rectangular enclosure of expanded PVC mounted on the back of the module. This enclosure has the same width and length dimensions as the module (see Table 1), and a proposed thickness of 27 mm. Preliminary calculations indicated that a fluid layer thickness of 50 mm or less would yield better heat exchange between the cooling fluid and the PV module, so the thickness of the aluminium frame was used for simplicity.

The design of the heat exchanger includes 16 valves that can work both as inlets and outlets, to allow experimenting with different configurations of forced convective flow of cooling water. This proposed PVT module design with multiple inlets and outlets and an unobstructed enclosure allows experimental versatility for testing different configurations within the same piece of equipment. This particular design was chosen as opposed to the implementation of fixed defined channels within the exchanger, given that such a design would require a different heat exchanger to be constructed for each configuration. Moreover, the proposed design allows the study of the effect of recirculation zones, as well as the effect of volumetric flow rate of cooling fluid on the flow pattern.

A total of 11 configurations are analysed in this paper in terms of heat removal, electrical generation and pressure drop. The location of the valves is indicated in Figure 3. The 11 analysed configurations are presented in Table 2, and one of them (B4) is graphically depicted in Figure 4 as an example. The graphical representation of the remaining configurations can be found in Appendix A. All the configuration schematics are accompanied by the expected flow lines. As the work presented in this paper does not include fluid dynamics simulations, the flow lines presented in Figure 4 are only for illustrative purposes, and are estimated based on the corresponding experimental thermographic image for each configuration. The configurations are classified into three subgroups, named by the manner in which the fluid enters the heat exchanger: from the bottom (B), from a single valve (S), and laterally (L).

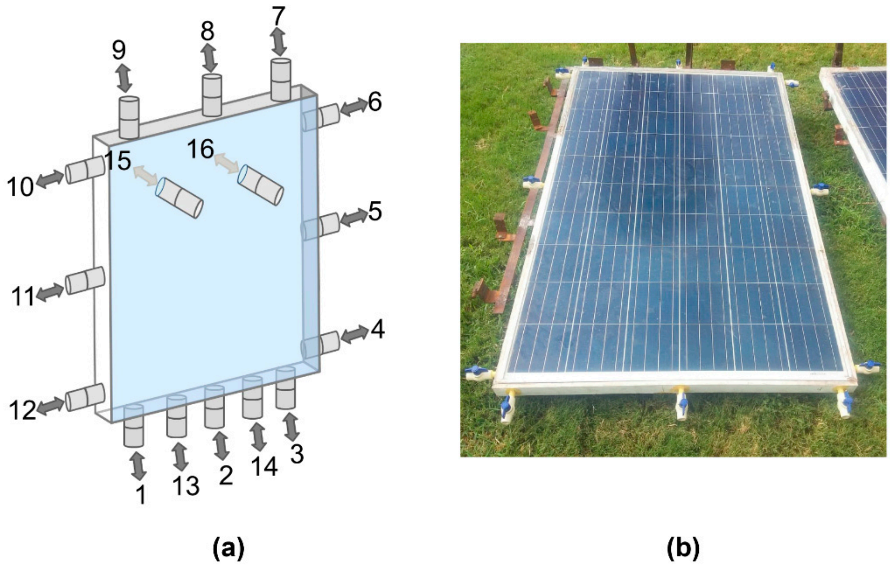

Figure 3. Constructed PVT heat exchanger indicating valve locations: (**a**) Schematic diagram, (**b**) Photograph of the experimental PVT module.

Table 2. Description of each of the heat exchange configurations analysed.

Configuration	Inlet (s)	Outlet (s)
B1	1, 2, 3, 4, 12, 13, 14	5, 11
B2	1, 2, 3, 4, 12, 13, 14	8
B3	1, 2, 3, 4, 12, 13, 14	6, 7, 9, 10
B4	1, 2, 3, 4, 12, 13, 14	15, 16
B5	1, 2, 3, 4, 12, 13, 14	9, 10
S1	3, 4	15, 16
S2	2	15, 16
S3	6, 7	9, 10
L1	3, 4	1, 9, 10, 11, 12
L2	11	3, 4, 5, 6, 7
L3	1, 9, 10, 11, 12	3, 4, 5, 6, 7

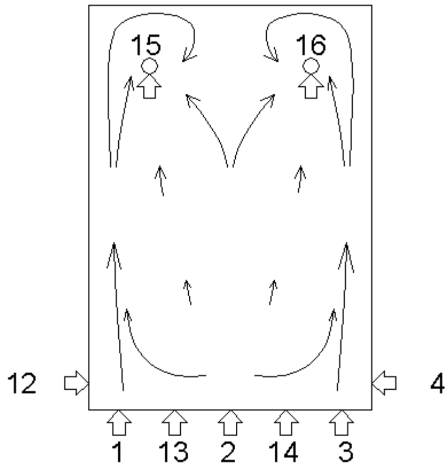

Figure 4. Schematic of heat exchange configuration B4, with inlets and outlets indicated by white arrows and expected flow lines (not calculated) indicated by black arrows.

2.3. PVT Module Performance Analysis

To analyse and characterise the thermal and electric performance, each proposed heat exchange configuration is tested in five PVT modules simultaneously while recording the weather conditions in terms of solar irradiation (G_s), wind speed (v_a), relative humidity (H_R), and ambient temperature (T_a). A regular (unmodified) PV module without a cooling system is also tested under the same conditions for comparison purposes. Each configuration test is done under two different cooling water flows (1 and 2 L min^{-1}). The cooling water is obtained from a nearby well, with an average salinity (w_b) of 500 ppm. The cooling water temperature is kept constant and all the tests are repeated three times. Figure 5a shows a photograph of the experiment, whereas Figure 5b shows a schematic of the experimental setup: a low-pressure (LP) pump makes water flow from a storage tank to the PVT modules, cooling them as they generate electricity, before it is finally discharged to another storage tank. The variables measured are the electrical power generated (P_e), the temperatures of the PV module (T_{PV}), the water inlet and outlet temperature at the panel (T_{wi} and T_{wo}, respectively), the conductivity of the cool water, and the pressure losses across the heat exchanger. The photovoltaic panel operates at maximum power conditions by connecting a micro-inverter to the electrical output of the panel. The micro-inverter injects the generated energy to the power grid, which draws a current and acts as an electrical load.

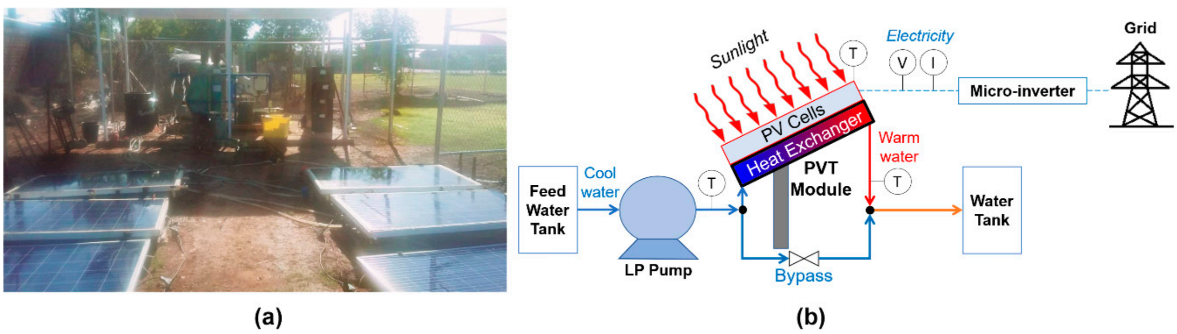

Figure 5. Experimental setup: (**a**) photograph, (**b**) schematic.

The environmental conditions (G_s, v_a, H_R and T_a) are monitored by a weather station. The water temperature and salinity at the PVT module inlet and outlet are measured using thermocouples and an electrical conductivity meter, respectively, and the cooling/feed water flow rate (Q_w) is manipulated using a bypass valve. The pressure losses are estimated from the total flow rate passing through the LP pump (Q_w plus the bypass) using the characteristic curve of the pump as supplied by the manufacturer, shown in Appendix B.

The PV module temperature distribution for each configuration is measured using a thermographic camera (model Flir i5) with a thermal sensitivity of <0.1 °C at 25 °C. The collected temperature data from each thermal image are then normalised, and the median, minimum, maximum, and standard deviation of the temperatures on the module surface are determined from these data. The heat removed from the module by the cooling water (q_w) is calculated using the following expression:

$$q_w = \rho_w Q_w C_{pw}(T_{wo} - T_{wi}) \tag{2}$$

where ρ_w and C_{pw} are the density and heat capacity of the cooling water, respectively. Cooling water properties are estimated using correlations reported by Sharqawy et al. [22] for density, heat capacity [23], and viscosity [24].

The heat removed by the heat exchanger (q_x) is modelled by:

$$q_x = U A_{px} \Delta T_{lm} \tag{3}$$

where A_{px} is the PV module area in contact with the cooling water (the heat exchange area), ΔT_{lm} is the logarithmic mean temperature difference between the module and the cooling water, and U is the global heat transfer coefficient for the heat exchanger.

It is considered that the heat removed from the module is the only heat absorbed by the cooling water, hence $q_w = q_x$, such that U can be obtained using Equations (2) and (3) for each heat exchange configuration:

$$U = \frac{\rho_w Q_w C_{pw}(T_{wo} - T_{wi})}{A_{px} \Delta T_{lm}} \tag{4}$$

As a non-uniform temperature distribution will lead to a decrease in electrical efficiency [16], we define the efficiency drop ($\Delta\eta$) as the difference between the efficiency expected at the mean temperature of the PV module (η_u) and the measured electrical efficiency under forced convective cooling (η_c):

$$\Delta\eta = \eta_u - \eta_c \tag{5}$$

The uniform efficiency at the mean temperature (η_u) is estimated from the experimental data obtained following the methodology described in Section 2.1. Finally, the relationship between efficiency drop is correlated to G_s, T_{PV}, U, Q_w and the standard deviation of the PV module temperature distribution (σ_T). The average values of $\Delta\eta$, Q_w, U, σ_T and maximum PVT module temperature ($T_{PV,max}$) are quantified for each test. These values are compared with a theoretical distribution of probabilities for continuous quantitative variables, using the t-student parametric distribution [25].

A linear regression between the parameters (Q_w, U, σ_T and $T_{PV,max}$) and the efficiency drop ($\Delta\eta$) is also performed to determine the influence of these parameters on the output performance of the system. This analysis assists in determining which parameter has a stronger effect on the electrical efficiency. If the Pearson correlation coefficient between $\Delta\eta$ and either Q_w, U, σ_T or $T_{PV,max}$ is less than -0.7, this would suggest that increasing the value of that parameter would improve the efficiency of the PVT module (by decreasing the efficiency drop), according to factorial simplicity index theory of Kaiser [26].

2.4. PVT-RO Simulation

A mathematical model of the combined PVT-RO system depicted in Figure 6 is implemented in MATLAB (Mathworks). The PVT-RO model (see Figure 7) consists of a solar PVT module, a high-pressure (HP) pump, and a RO membrane module. Some outputs of the PVT model (Q_b and P_e) are inputs to the HP pump model that determines the RO feed pressure (p). The RO model then takes inputs from both the PVT and HP pump models to determine the permeate variables (Q_p and w_p). All models are considered to operate under quasi-steady state, under the assumption that any dynamic changes to the operating conditions (changes in weather, location of the sun, etc.) occur at a slower time scale than necessary to reach thermal equilibrium in both the PVT and the RO modules.

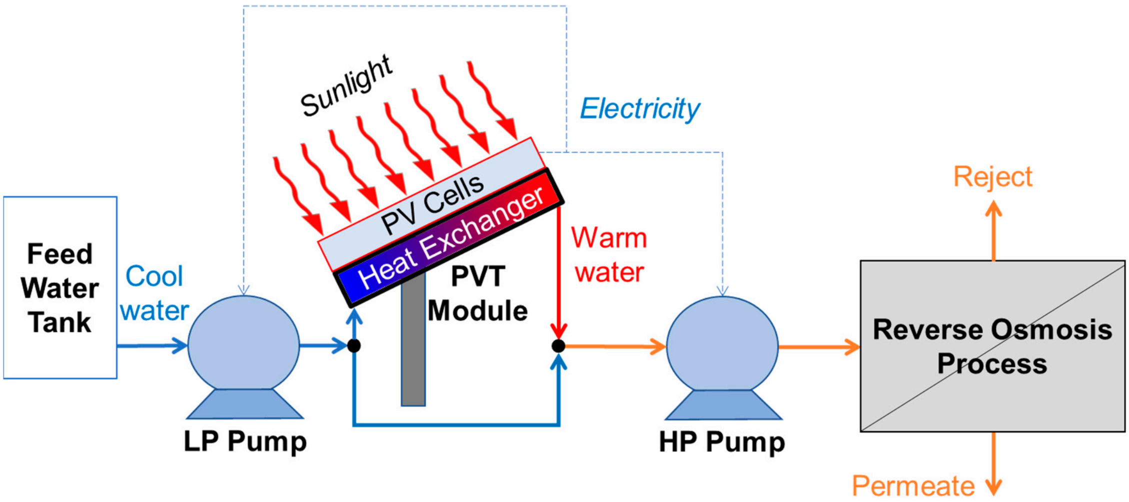

Figure 6. Schematic diagram of the PVT-RO system.

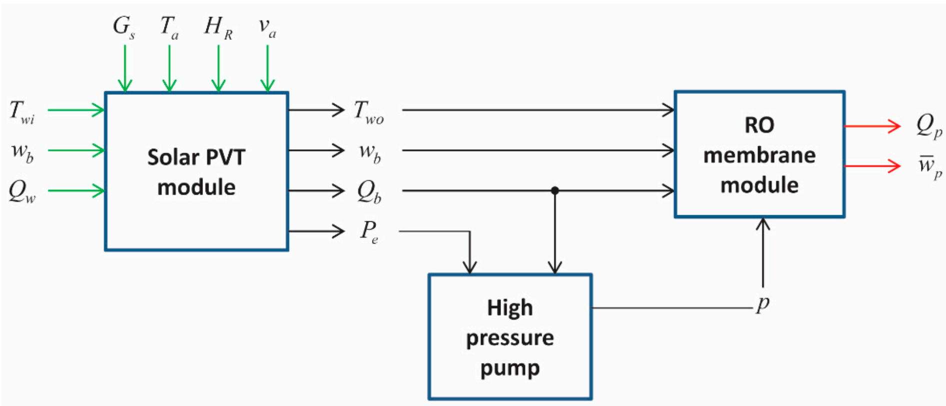

Figure 7. Variable map and block diagram of the mathematical model of the PVT-RO system, where green arrows are inputs, black arrows are intermediate variables, and red arrows are outputs. Refer to the nomenclature for variable descriptions.

2.4.1. Solar PVT Module

The PVT model consists of a system of non-linear equations, solved using a Newton-Raphson iterative method. The energy balance around the PVT module is given by:

$$E_{PV} = q_s - q_a - q_r - q_x - P_{eo} \tag{6}$$

where E_{PV} is the rate of net energy input into the PVT module, q_s is the energy input from solar irradiation, q_a is the thermal energy removed by convective heat transfer with the wind, q_r is the cooling via radiative heat transfer with the sky, and P_{eo} is the electrical power output of the PVT module. The terms on the right-hand side of Equation (6) are estimated by Equation (3) and by:

$$q_s = \left(G_{beam} f_\theta \cos\theta + G_{dif}\right)\alpha_s A_{PV} \tag{7}$$

$$q_a = h_a A_{pa}(T_p - T_a) \tag{8}$$

$$q_r = A_{PV}\sigma\varepsilon\left(T_p^4 - T_{sky}^4\right) \quad (9)$$

$$P_{eo} = \eta_c A_{PV}\left(G_{beam} + G_{dif}\right) \quad (10)$$

where G_{beam} and G_{dif} are the beam and diffuse solar irradiation, α_s and A_{PV} are the solar absorptivity and the active area of the PV module, f_θ is the angular dependence of solar absorptance [27], θ is the incidence angle between the PV module and the sun, h_a is the wind heat transfer coefficient, A_{pa} is the module area in contact with the wind, σ is the Stefan-Boltzmann constant, T_{sky} is the sky temperature, and ε is the emissivity of the PV module. Further details and auxiliary expressions used in computing the values used for Equation (7) through Equation (10) are provided in Appendix C.

For the cooling water, the energy balance considers only the heat exchange with the panel that leads to an increase in water temperature, and the sensible heat absorbed by the water as given by Equation (2) The energy balance for the cooling water is then:

$$E_w = q_x - q_w \quad (11)$$

where E_w is the rate of net energy input into the cooling water. At steady state, both rates of energy input (E_{PV} and E_w) should be equal to zero, leading to a system of two non-linear equations:

$$\begin{aligned} E_{PV}\left(T_p, T_{wo}\right) &= 0 \\ E_w\left(T_p, T_{wo}\right) &= 0 \end{aligned} \quad (12)$$

These non-linear equations represent the energy balances around the PV module-heat exchanger system (i.e., the PVT module). The weather conditions and the inlet cooling water flow properties are inputs to this system, and the outputs consist of the outlet water flow properties and electrical power (P_e), as depicted in Figure 7.

However, not all of the electrical power generated by the PVT module (P_{eo}) is available for the HP pump. This because a non-negligible amount of power is required to force the flow of cooling water across the PVT heat exchanger. In order to account for this, the low-pressure pumping power (P_{LP}) is estimated as:

$$P_{LP} = \frac{\Delta p_{PVT} Q_w}{\eta_{LP}} \quad (13)$$

where Δp_{PVT} is the pressure drop across the heat exchanger in the PVT module and η_{LP} is the energy efficiency of the LP pump (assumed as 75% for a fit-for-purpose pump). The power available for the HP pumps is then taken to be:

$$P_e = P_{eo} - P_{LP} \quad (14)$$

2.4.2. HP Pump

The HP pump mathematical model is a series of multilinear regressions fitted to the technical datasheet of a HP DC pump (SunPumps SIJ 3.1-1500P-225 BL). The inputs to this model are the PV power output (P_e) and the cooling water outlet flow rate (Q_{wo}). The model calculates the maximum water pressure (p) that can be provided by the HP pump to the RO module under those conditions. More details are provided in Appendix C.

2.4.3. RO Membrane Module

The RO modelling in this work largely follows the approach of Toh et al. [28] and Bartholomew & Mauter [29], but with the additional complexity of allowing for the fluid properties (density, viscosity, heat capacity) and membrane properties (water and salt permeance) to vary with temperature as well as with salinity. At its core, the RO model is a combination of two simpler models: a non-linear algebraic equation system for determining the local permeate flux, and a system of non-linear ordinary differential equations (ODEs) describing the evolution of the unidimensional profiles of the variables (flow velocity, concentration, temperature, and pressure) along the membrane module, as depicted in Figure 8. The former is solved via the simple fixed-point iteration method [30], while the latter is solved by a Runge–Kutta type algorithm.

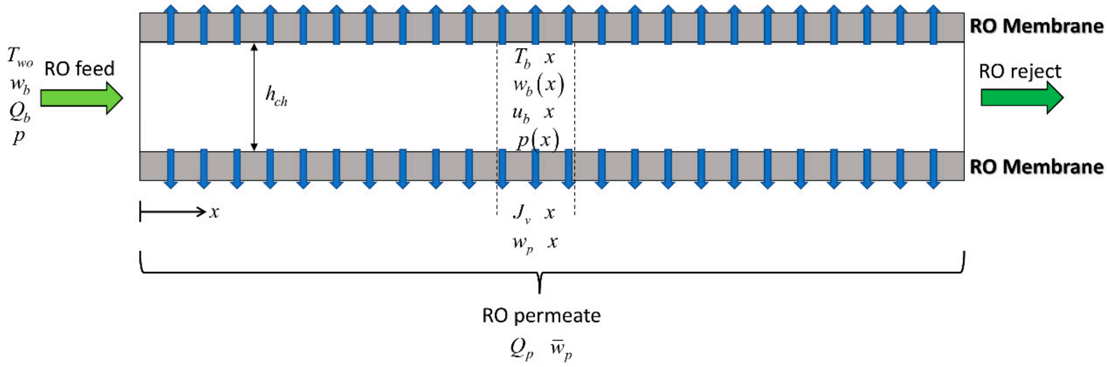

Figure 8. Schematic diagram of the unidimensional RO model, showing inputs, outputs and profile variables. Refer to the nomenclature for variable descriptions.

The local volumetric permeate flux (J_v) at each point along the RO membrane module (x-direction) is estimated using the Kedem–Katchalsky–Merten equation [31]:

$$J_v = \frac{\Delta p_{tm} - (\pi_m - \pi_p)}{\mu R_m} \tag{15}$$

where Δp_{tm} is the transmembrane pressure difference between the feed and permeate channels, π_m and π_p are the osmotic pressure on the feed and permeate side of the RO membrane, μ is the fluid viscosity and R_m is the membrane resistance. The effect of changes in water temperature is explicitly considered to affect the fluid viscosity, as well as the osmotic pressure following the van't Hoff equation for NaCl:

$$\pi = 2\frac{\varphi R_g w \rho T}{M_s} \tag{16}$$

where φ is the osmotic coefficient, R_g is the universal gas constant and M_s is the molar mass of NaCl. The temperature dependence of osmotic pressure is explicit in Equation (16), but it is also implicit as φ and ρ are also considered to be temperature dependent [22]. The effect of temperature on the membrane resistance and salt permeance were determined experimentally for a commercial DuPont BW30 membrane. A non-linear system arises from the coupling of permeate flux and membrane surface salinity (w_m) due to the effect of concentration polarisation [28]:

$$\Gamma = \frac{w_m - w_p}{w_b - w_p} = \exp\left(\frac{J_v}{k_{mt}}\right) \tag{17}$$

where Γ is the concentration polarisation modulus and k_{mt} is the mass transfer coefficient on the membrane surface.

Finally, the model describing the profiles along the membrane module is based on mass and energy balances under steady-state non-isothermal conditions, and neglecting longitudinal dispersion. This results in the following system of ODEs:

$$\frac{du_b}{dx} = -\frac{2J_v\rho_p}{h_{ch}\rho_b} - \frac{u_b}{\rho_b}\left(\frac{\partial\rho_b}{\partial x}\frac{dw_b}{dx} + \frac{\partial\rho_b}{\partial x}\frac{dT_b}{dx} + \frac{\partial\rho_b}{\partial x}\frac{dp_b}{dx}\right) \tag{18}$$

$$\frac{dw_b}{dx} = \frac{2J_v\rho_p}{h_{ch}u_b\rho_b}R_{obs}w_b \tag{19}$$

$$\begin{aligned}\frac{dT_b}{dx} &= \frac{2J_v\rho_p}{h_{ch}u_bC_{p,b}\rho_b}\left(\Delta H_{s,r}R_{obs}w_b + \Delta H_{tm} + \Delta H_{p,tm}\right)\\ &-\frac{\Delta H_{s,r}}{C_{p,b}}\frac{dw_b}{dx} - \frac{1}{C_{p,b}\rho_b}\left(1-\frac{T_b}{\rho_b}\frac{\partial\rho_b}{\partial T_b}\right)\frac{dp_b}{dx}\end{aligned} \tag{20}$$

$$\frac{dp}{dx} = -\frac{2\rho u_b^2}{d_h\epsilon^2}f \tag{21}$$

where x is the direction along the membrane module length, the subscript b represents the feed channel bulk conditions, h_{ch} is the membrane channel height (taken to be equal to the spacer thickness), ϵ is the feed channel void fraction (the volume other than the spacer mesh), d_h is the hydraulic diameter of the spacer-filled feed channel, f is the Fanning friction factor, R_{obs} is the local observed rejection, and $\Delta H_{s,r}$ = 66.2 kJ kg^{-1} is the specific enthalpy change of solution for NaCl at reference conditions of T_r = 25 °C and p_r = 1 atm. The transmembrane temperature-enthalpy change ($\Delta H_{T,tm}$), and transmembrane pressure-enthalpy change ($\Delta H_{p,tm}$), are respectively defined as follows:

$$\Delta H_{T,tm} = \int_{T_r}^{T_b}\left[C_p(T,\ w_b, p_r) - C_p(T,\ w_p, p_r)\right]dT \tag{22}$$

$$\Delta H_{p,tm} = \int_{p_p}^{p_b}\frac{1}{\rho(T_b,\ w_b, p)}\left[1-\frac{T_b}{\rho(T_b,\ w_b, p)}\left(\frac{\partial p}{\partial T}\right)_{p,w_b}\right]dp \tag{23}$$

Equations (18)–(21) are integrated along the membrane module length (see Figure 8) to obtain the total permeate flow (Q_p) and permeate salinity (w_p). Further details regarding the estimation of permeate flow and auxiliary equations are presented in Appendix C.

All simulations assume a quasi-steady state using data from a local weather station in Ciudad Obregon, Mexico (27°29′35.2″ N 109°58′10.7″ W), for summer (24 July 2018), autumn (20 October 2019) and winter (3 January 2020) conditions. The weather data for these dates and location is presented in Appendix D. Three simulation scenarios are considered: Scenario 1 "Without cooling" emulates the electrical generation of a regular PV-RO plant for comparison; Scenario 2 "Continuous cooling" emulates the performance of a PVT-RO plant incorporating the different heat exchange configurations considered in this paper; and Scenario 3 "Max production" selects the best performance out of scenarios 1 and 2 depending on the time of the day and environmental conditions, which results in the maximum possible permeate production for the day under consideration. All scenarios assume the same dimensions and characteristics of the experimental PVT module, and the simulated RO membrane is based on the BW30-8040 DuPont FilmTec module for brackish water [32]. The parameter values considered are summarised in Table 3.

To simulate the behaviour of the PVT-RO system under the different cooling configurations in Scenario 2, the simulation parameters are adjusted to match each heat exchange configuration experimental data as follows: (1) the experimental value of U is used as an input to the PVT model, and (2) the dependency of $\Delta\eta$ on the operating conditions (G_s, T_{PV} and Q_w) and cooling configuration is incorporated. Moreover, to guarantee that 1 and 2 L min^{-1} are flowing through each of the modules while keeping the same feed flow rate into the RO module (Q_b), half of the feed flow rate is assumed to bypass the PV panels at Q_w = 1 L min^{-1}.

Table 3. Simulated PVT-RO unit dimensions and characteristics.

Parameter	Value	Units
Membrane length [32]	0.955	m
Membrane area [32]	2.8	m^2
Feed channel height (h_{ch}) [33]	0.77	mm
Feed channel void fraction (ϵ) [33]	0.89	mm
Feed channel hydraulic diameter (d_h) [33]	0.95	mm
PV module area (A_p)	1.52	m^2
Cooling water film thickness	0.027	m
Cooling water inlet temperature (T_{wi})	25	°C
Number of PVT modules	4	modules
Cooling water inlet salinity (w_b)	500	ppm
Total water flow (Q_b)	8	L min^{-1}

3. Results and Discussion

3.1. PV Module Characterisation

Experimental tests showed that the behaviour of the PV modules varies from the data reported by the manufacturer. This is due to manufacturing defects, so it is recommended to generate a specific I-V curve for the PV panel used under real conditions. A PV module efficiency loss of 0.7% for each 10 °C increase in uniform temperature was observed. Figure 9 shows the I–V curve obtained in the field at T_{PV} = 59.2 °C and G_s = 1000 W m^{-2}. The real efficiency obtained is 16.02%, about 0.58% lower than that reported by the manufacturer (see Table 1).

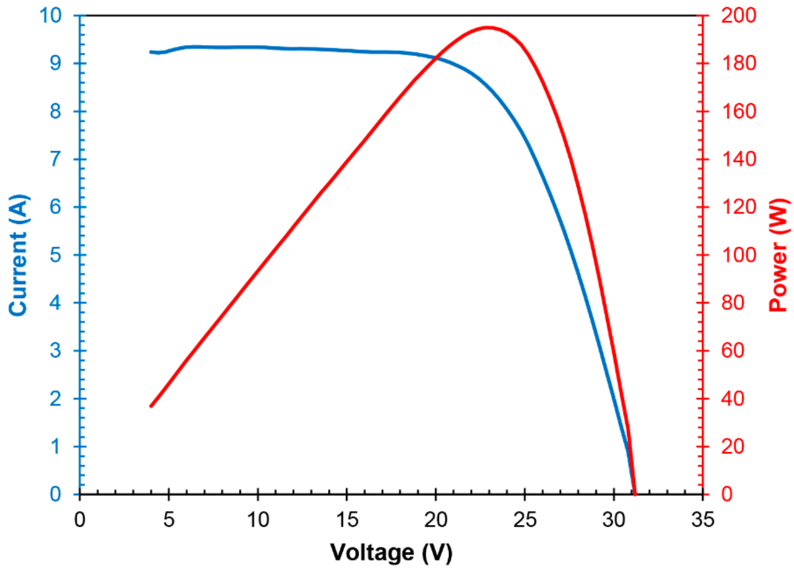

Figure 9. Measured I-V curve at T_{PV} = 59.2 °C and G_s = 1000 W m^{-2}, for the PV modules used in this work.

Regarding the effect of temperature, Figure 10 shows that the electrical efficiency significantly decreases due to increases in temperature. A significant (95% confidence) negative correlation is observed for the relationship between these variables (r = 0.92, $p < 0.001$). The degree of goodness of fit was high (R^2 = 0.85) for the linear regression model:

$$\eta_u = 0.1777 - 7.034 \times 10^{-4}\, T_{PV} \tag{24}$$

where T_{PV} is the uniform PV module temperature in °C.

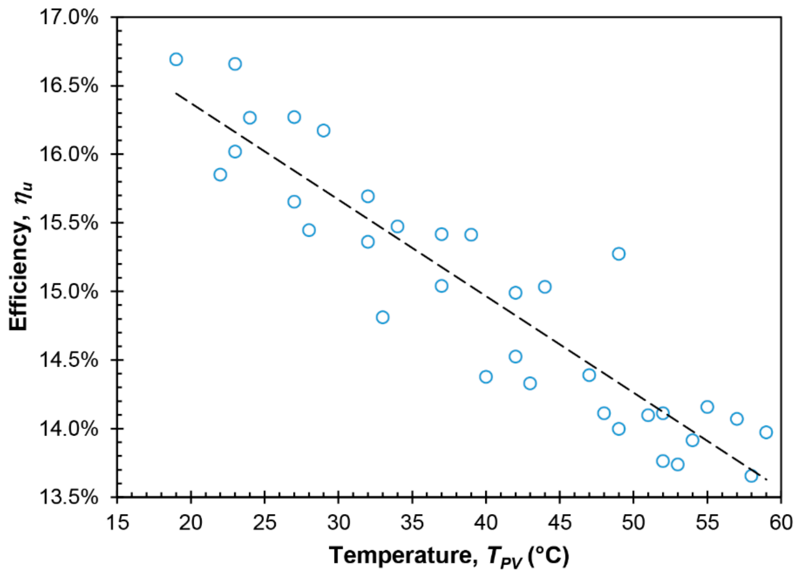

Figure 10. Effect of temperature on efficiency for the PV module.

3.2. Experimental Results of the PV Module Cooling Configurations

In order to remove the biases and effects introduced by the different environmental conditions at the time of testing each of the different configurations, the temperature distribution for each configuration was first normalised as follows:

$$T_{PV,n} = \frac{\overline{T}_{PV,NC} - T_{PV,C}}{\overline{T}_{PV,NC} - \overline{T}_{PV,C}} \quad (25)$$

where the subscript n represents the normalised temperature, NC refers to the module that is not cooled, and C refers to the water-cooled module. The overbars represent the arithmetic mean of the temperature for the corresponding module. Subtracting the temperature of the cooled module from that of the non-cooled module removes some of the bias associated with higher or lower solar irradiation during measurement. By this definition, the normalised temperature should have an arithmetic mean of 1.

With respect to the temperature distribution in the PVT, Figure 11 shows the ranges of normalised temperatures for each heat exchange configuration, indicating the maximum and minimum temperatures, as well as the sizes of the central interquartiles and the median. This information can help determine which configurations lead to a more uniform temperature distribution. Group B has more uniform and compact ranges than groups S and L. Conversely, group S presents the largest ranges of temperatures, particularly configurations S1 and S3.

The L group shows the configuration with the smallest normalised temperature range (L2), although there is more variability in the ranges within the L group, this compared to the B group. The configurations with the smallest normalised temperature range are the ones that lead to a more uniform temperature, being this the condition with $\Delta\eta$ close to zero.

The results of the experimental measurements of efficiency drop for the PVT modules are shown in Figure 12. In the graphs in this figure, $\Delta\eta$ is plotted against maximum temperature ($T_{PV,max}$), overall heat transfer coefficient (U) and the standard deviation of the temperature distribution (σ_T). In addition, the two values of water flow rate (Q_w) for each configuration are joined by a line, with a circle indicating the larger flow rate of Q_w = 2 L min^{-1}.

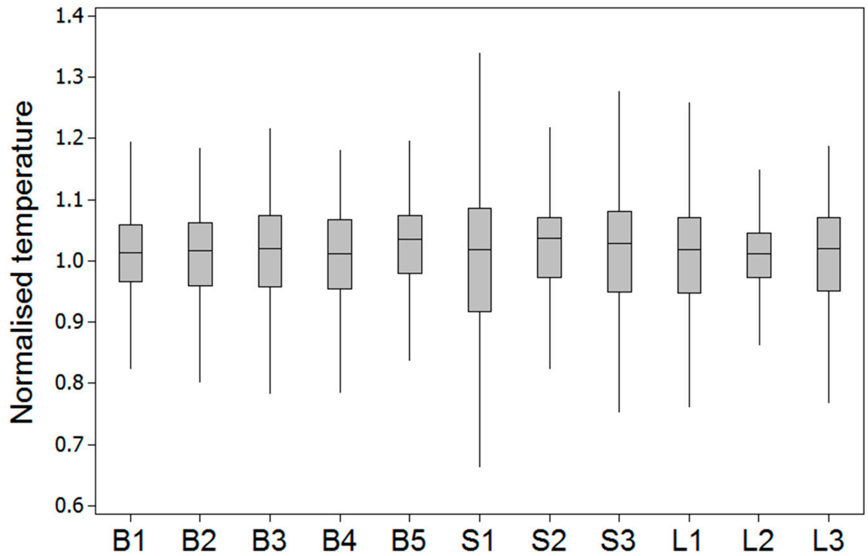

Figure 11. Ranges of observed normalised temperatures for each heat exchange configuration, with the median and quartiles indicated.

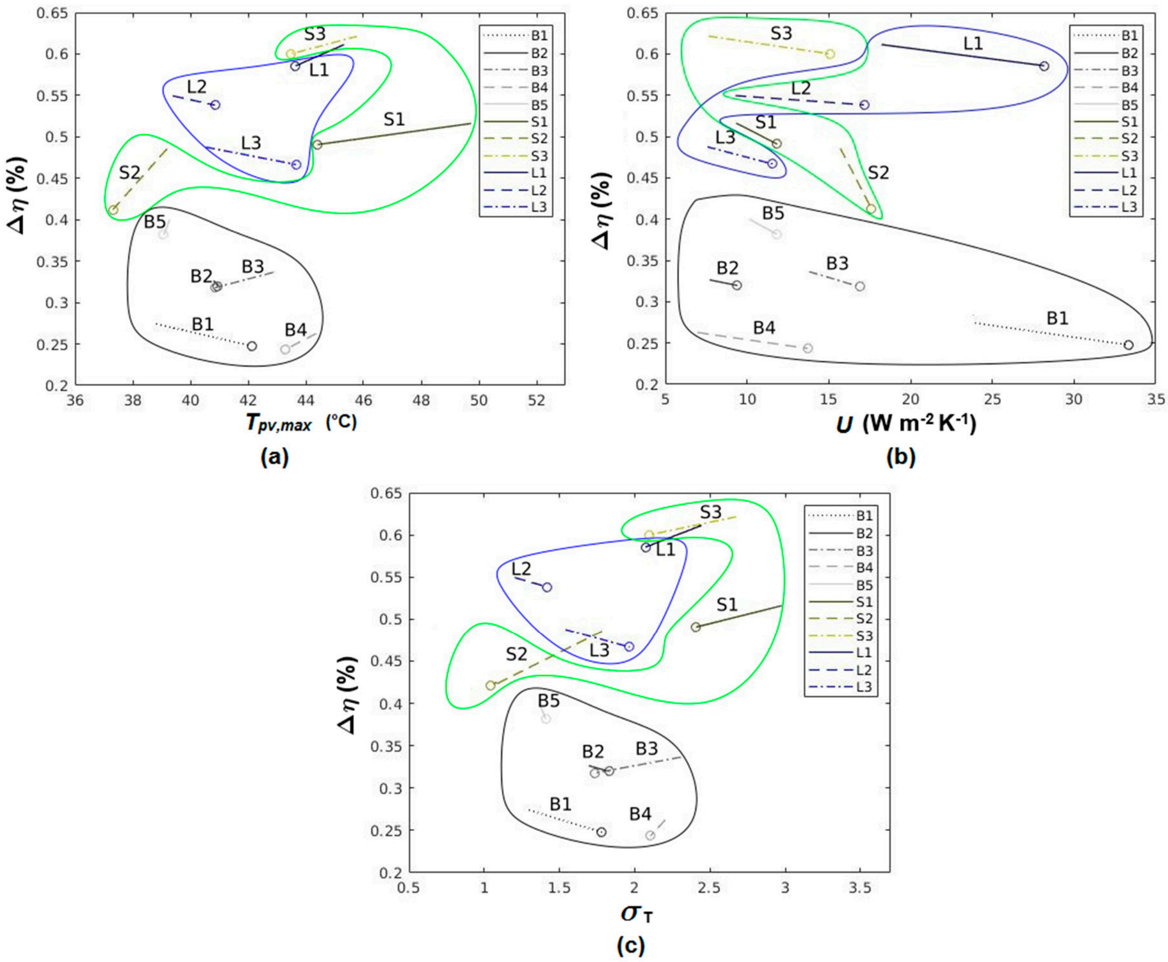

Figure 12. Effect on the efficiency drop ($\Delta\eta$) of: (**a**) maximum PV module temperature ($T_{PV,max}$), (**b**) overall heat transfer coefficient (U), and (**c**) standard deviation of temperature distribution (σ_T). Data points for the same configuration are joined by a line, with the unmarked ends of the lines representing the data at Q_w = 1 L min^{-1}, and the ends marked with a circle representing the data at Q_w = 2 L min^{-1}.

Configuration types B, S and L are indicated by similar colour groups in Figure 12. This is done to visualise the similarities between the members of each group. In the case of group B, it can be seen that the configurations are grouped on the lower part of each graph, where $\Delta\eta$ is lower and therefore closer to the efficiency of the photovoltaic panel at uniform temperature. This suggests that configurations belonging to group B result in best performance in terms of temperature distribution, leading to lower efficiency drop. It can also be seen in Figure 12b that, for all configurations, increasing Q_w reduced the efficiency drop and increased U.

However, Figure 12a,c indicate that a larger temperature range (i.e., a larger $T_{PV,max}$) or a larger temperature variability (i.e., a larger σ_T) do not necessarily lead to larger efficiency drops in the configurations tested. This is particularly evident for configurations B1, L2 and L3, for which $T_{PV,max}$ and σ_T increase as Q_w is increased, but $\Delta\eta$ is reduced. Nevertheless, if the analysis is focused on the overall data, a general tendency can be seen that $\Delta\eta$ is larger for configurations with larger σ_T and larger $T_{PV,max}$. On the flipside, this general tendency is not observed for the relationship between $\Delta\eta$ and U. These observations are corroborated by the overall Pearson correlation coefficients presented in Table 4, and suggest that, although in general a better temperature distribution and lower temperature range will lead to less efficiency losses, for any particular configuration heat removal drives efficiency drop.

Table 4. Pearson correlation coefficients between efficiency drop ($\Delta\eta$) and each of the studied input parameters, for each configuration and for the overall data set. Highly significant correlation coefficients are highlighted in bold.

	Pearson Correlation Coefficient between $\Delta\eta$ and:			
Configuration	Q_w	U	σ_T	$T_{PV,max}$
B1	−0.57	0.67	−0.27	**−0.82**
B2	−0.50	0.31	0.59	0.58
B3	−0.62	0.05	**0.70**	**0.83**
B4	**−0.73**	−0.50	−0.45	−0.40
B5	−0.31	−0.68	−0.29	−0.28
S1	**−0.83**	−0.46	−0.34	−0.15
S2	**−0.93**	−0.22	0.21	0.04
S3	−0.35	−0.68	0.53	0.31
L1	−0.51	−0.20	0.64	0.52
L2	**−0.79**	−0.67	0.16	0.40
L3	−0.48	−0.18	**−0.92**	**0.90**
Overall	−0.10	−0.07	0.18	0.22

To quantify the trends observed in Figure 12, the statistical relationships between the variables in that figure are presented in Table 4, which shows the Pearson correlation coefficients between the efficiency drop for each configuration and the operating parameters studied, as well as the overall correlations. It can be seen that Q_w has a negative correlation with $\Delta\eta$ in all configurations and overall. This means that increasing feed flow rate generally led to an increase in electrical efficiency, confirming the trends observed in Figure 12b. Configurations B4, S1, S2, and L2 show a correlation coefficient magnitude ≥ 0.7, which classifies as highly significant behaviour according to the factorial simplicity index.

On the other hand, the heat transfer coefficient (U) did not show a highly significant behaviour in affecting the efficiency drop overall. Although for most configurations an increase in U was slightly correlated with a decrease in efficiency drop (a trend also observed in Figure 12b), the statistical results suggest that increasing heat transfer efficiency will not necessarily lead to higher energy generation. The results of configurations with a positive correlation may be related with the input cooling fluid being distributed vertically with less uniform heat extraction inside the PVT module. Since the cooling fluid residence time is low, this is probably due to the cooling fluid being directed to vertical outlets placed partially aligned with the inputs. The negative signs may be attributed to the fact that the temperature of the cooling fluid is increased more along flow lines with a longer residence time inside the PVT module. This is due to the fact that the direction of the water changes, as inputs are not aligned with outputs, leading to recirculation zones.

As regards the effect of σ_T on the efficiency drop, the L3 configuration presents a correlation coefficient ≤ -0.7 (r = -0.92). This result is probably due to the multiple inlets and outlets being aligned horizontally and the PV cells in the module being wired vertically and in parallel with each other, thus the temperature variation along each series of PV cells is minimal. The negative correlation can be explained by the fact that a higher temperature variability is mostly associated with a larger water temperature increase due to more cooling of the PV module, hence reducing the efficiency drop. On the other extreme, the B3 configuration has a correlation coefficient ≥ 0.7. This could indicate that the fluid tends flow largely in the vertical direction, resulting in a large temperature difference along the PV cells wired in series, therefore reducing the electrical efficiency in the photovoltaic panel.

The correlation coefficients for $T_{PV,max}$ show that configuration B1 has a highly significant coefficient ≤ -0.7 (r = -0.82). This can probably be attributed to the symmetric vertical flow of cooling water. Configurations B3 and L3 also show highly significant correlation coefficients ≥ 0.7. This is probably because the multiple outlets are geometrically spaced from each other.

3.3. PVT-RO Modelling Results

The experimental data for heat transfer (U) and efficiency drop is incorporated into the PVT-RO model described in Section 2.4. This in order to estimate the energy generated by the PVT modules under different cooling configurations and without forced cooling, as well as the energy available to be used in the RO desalination process (E_e). The model then uses these results to predict the volume of water produced by the PVT-RO hybrid system (Vol_p) and the salinity of the permeate (w_p). Simulation results for two representative dates are presented in Tables 5 and 6.

The model results for 20 October (Table 5) show that B1 has the best performance of all configurations tested under continuous cooling at Q_w = 1 L min^{-1}, both in terms of energy and permeate production. For the tests under continuous cooling at Q_w = 2 L min^{-1}, the energy available is reduced in comparison with the lower flow rate, and therefore the production of permeate water is also reduced. The model results for 24 July (Table 6) also show that B1 results in the best performance for both Q_w = 1 L min^{-1} and Q_w = 2 L min^{-1}.

Table 5. Simulation results for PVT-RO hybrid system power generation and water production, based on weather data for 20 October 2019.

Scenario	Vol_p (m^3)	E_e (Wh)	w_p (ppm)	Vol_p (m^3)	E_e (Wh)	w_p (ppm)	Vol_p (m^3)	Increase (%)	Vol_p (m^3)	Increase (%)
WithoutCooling	1.296	884	4.3							
Scenario	**Continuous Cooling**						**Max Production**			
Q_w	**1 L min^{-1}**			**2 L min^{-1}**			**1 L min^{-1}**		**2 L min^{-1}**	
B1	1.650	913	8.4	1.002	636	8.1	1.650	27.5%	1.296	-
B2	1.452	879	6.2	0.834	603	6.3	1.458	12.6%	1.296	-
B3	1.506	888	6.8	0.936	622	7.2	1.506	16.4%	1.296	-
B4	1.404	872	5.8	0.906	614	6.9	1.410	9.2%	1.296	-
B5	1.440	875	6.3	0.888	617	6.8	1.440	11.5%	1.296	-
S1	1.410	869	6.1	0.906	627	6.8	1.416	9.7%	1.296	-
S2	1.512	888	7.0	0.966	635	7.2	1.518	17.3%	1.296	-
S3	1.422	874	6.0	0.930	626	7.0	1.428	10.5%	1.296	-
L1	1.512	882	7.1	1.026	649	7.8	1.512	17.0%	1.296	-
L2	1.398	866	6.1	0.954	634	7.2	1.410	9.0%	1.296	-
L3	1.356	857	5.8	0.882	618	6.8	1.368	5.9%	1.296	-

Table 6. Simulation results for PVT-RO hybrid system power generation and water production, based on weather data for 24 July 2018.

Scenario	Vol_p (m^3)	E_e (Wh)	w_p (ppm)	Vol_p (m^3)	E_e (Wh)	w_p (ppm)	Vol_p (m^3)	**Increase (%)**	Vol_p (m^3)	**Increase (%)**
Without Cooling	2.784	1247	20.4							
Scenario	**Continuous Cooling**						**Max Production**			
Q_w	**1 L min^{-1}**			**2 L min^{-1}**			**1 L min^{-1}**		**2 L min^{-1}**	
B1	3.240	1336	39.4	2.508	1054	23.1	3.240	16.5%	2.838	1.9%
B2	3.000	1265	30.4	2.148	983	16.8	3.006	8.2%	2.784	-
B3	3.066	1281	32.9	2.352	1017	19.7	3.078	10.6%	2.784	-
B4	2.958	1261	29.2	2.304	1010	19.3	2.970	6.8%	2.784	-
B5	2.988	1260	30.0	2.256	1002	18.2	2.994	7.8%	2.784	-
S1	2.958	1252	29.0	2.286	1012	18.5	2.976	7.0%	2.784	-
S2	3.096	1293	34.7	2.430	1041	21.4	3.102	11.6%	2.790	0.3%
S3	3.054	1306	36.4	2.454	1054	23.1	3.066	10.1%	2.814	1.3%
L1	3.060	1269	31.6	2.478	1041	20.8	3.072	10.4%	2.808	1.0%
L2	2.934	1242	27.7	2.352	1019	19.2	2.946	6.0%	2.784	0.0%
L3	2.850	1218	24.5	2.184	986	16.7	2.874	3.4%	2.784	-

An important factor to be considered in addition to the amount of water produced is the salinity of the permeate flow, as this has implications in terms of the potential applications for PVT-RO. Observed rejection for all the configurations tested range around 92% to 95% in the summer, when the lowest values are observed. Importantly, the configuration with the largest water production (B1) presents the lowest rejection (92%) and largest permeate salinity (39 ppm) from a feed water salinity of 500 ppm. This is expected, as Figure 12b shows that configuration B1 yields the largest heat transfer coefficient, and hence the highest RO feed water temperature. A higher temperature feed is known to reduce salt rejection as well as increasing water permeance for RO and other osmotic separation membranes [19,34].

Another effect that can be observed in Figure 12 is a lower permeate salinity at the larger cooling water flow rate of Q_w = 2 L min^{-1}. This effect can be related to the lower available pumping energy at this higher cooling rate. Although in general, for all configurations, operating at the larger flow rate results in a lower efficiency drop (see Figure 13), the larger pressure drop across the PVT heat exchanger results in less energy available (E_e) for the RO HP pump. This in turn leads to a lower operating pressure for the RO module, which results in a lower permeate flux, but also in less concentration polarisation as predicted by Equation (17). This latter effect also leads to a lower membrane surface salinity, and thus less salt passage through the RO membrane and ultimately lower permeate salinity.

Figure 13 shows the variation in water production under the three scenarios simulated, that is, under continuous cooling, without cooling, and under maximum production conditions. This latter scenario uses cooling only when it is predicted to result in greater water production than without cooling. These data are presented for the day in autumn for configuration B1 at Q_w = 1 L min^{-1} (Figure 13a) and at Q_w = 2 L min^{-1} (Figure 13b). For the lower flow rate, the scenario without cooling yields more permeate water during the early morning and late afternoon hours, but the cooling scenario results in greater permeate production for most of the day. Therefore, a hybrid operation consisting of turning the cooling system on and off is proposed to maximise the generation of electricity and hence maximising the water production. For this case, maximum production would be achieved if the cooling system is engaged only when the increase in energy generation due to the increase in efficiency overcomes the trade-off with energy losses due to pressure drop in the heat exchanger, which occurs roughly between 9:00 h and 15:30 h. On the other hand, for the larger water flow rate, the cooled scenario never overcomes the increased energy losses due to pressure drop, so for that case it is not convenient to engage the cooling system on that particular autumn day.

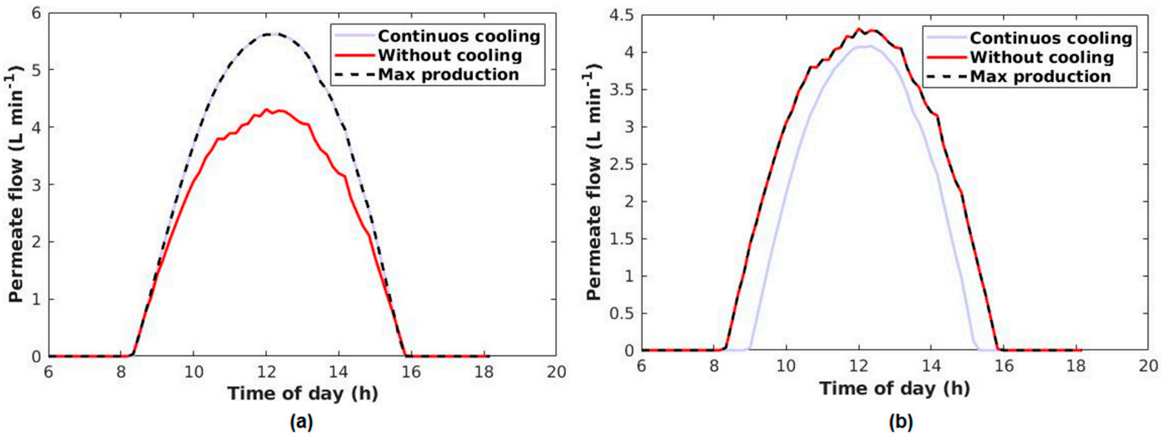

Figure 13. Simulated daily water generation for 20 October 2019, using configuration B1 at: (**a**) Q_w = 1 L min^{-1}; (**b**) Q_w = 2 L min^{-1}.

The data presented in Tables 5 and 6 and Figure 13 are for simulation results using weather measurements from the autumn and summer seasons. Nonetheless, simulations were also carried out using data from the winter season (3 January 2020). However, the winter simulations indicated less permeate production under forced cooling regardless of the water flow rate. This because the power required to overcome pressure losses in the PVT heat exchanger is larger than the gains in energy production, resulting in less available power for the HP pump. Hence, the winter data are not presented in this paper.

4. Conclusions

The results presented in this paper confirm that it is possible to achieve larger PV energy production as well as more RO permeate by cooling the PV modules using the RO feed water, achieving the expected synergies. However, pumping energy is required to force the flow of cooling water across the heat exchange surface with the PV module, which presents a trade-off that limits the conditions under which it is advisable to operate this cooling. This because the efficiency gains may not be sufficient to cover the required pumping energy, resulting in less energy available to operate the RO unit despite larger energy generation by the PV module.

The results of the statistical analysis of the operating parameters for the PVT-RO system yield some insights into the characteristics of the proposed cooling configurations that result in greater electrical efficiency gains. The main objective of the forced convective cooling through heat exchange should be to remove as much thermal energy as possible without incurring in significant efficiency drop due to a non-uniform temperature distribution. Although higher heat transfer coefficients may maximise the efficiency for a particular configuration, this should not be the only consideration.

On the other hand, the way in which the fluid enters the PVT module was seen to be one of the main drivers of efficiency drop, with configurations from group B leading to better performance. This group was characterised by symmetric vertical flow feed and multiple inputs close to each other. This can be related to PV cells being grouped in series by the manufacturer in vertical direction. Moreover, the cooling configurations that presented the best electrical performance were those that forced the fluid to circulate in a continuous direction from inlet to outlet, either horizontal or vertical, preventing recirculation. Future complementary investigations are recommended, in which the implementation of flow channels inside the heat exchanger is contemplated, as well as the optimisation of cooling water flow rate.

In addition, the PVT water outlet temperature was shown to influence the RO system, so it is imperative to consider the PVT-RO system as a whole when selecting the cooling configuration to be used. Thus, it can be concluded that out of the configurations tested, the characteristics of the B1 configuration are the best suited for the production of permeate water under the conditions proposed by this study. This configuration resulted in the highest percentage increase in permeate water compared to not using a cooling system, leading to a predicted 16.7% increase in production during summer and a 27% increase in production during autumn, growing to a 27.5% increase in autumn when only engaging the cooling system when the conditions for an increase in production is observed.

Although increasing the cooling water flow rate generally leads to a decrease in efficiency drop in the PV modules, the energy losses due to pressure drop in the heat exchanger also increase substantially, such that the gains in efficiency do not compensate for the energy losses. For this reason, it is recommended to run the system at lower cooling water flow rates. It is important to point out that the present investigation did not determine the optimal water flow rate for the proposed system. Hence, this is an area of opportunity for future studies. Nevertheless, the results are conclusive for lower cooling water flow rates in the ranges of the proposed experiment.

The decrease in rejection and higher permeate salinity when using feed water to cool the PV modules may be a limitation for applications with high salt content, such as seawater RO for which feed salinity is usually around 35,000 ppm. For that application, a relatively low rejection of 92% may lead to an unacceptably high permeate salinity. Therefore, the relevance of PVT-RO should be analysed according to the specific case and need. In addition, for seawater applications the feed osmotic pressure is higher, which would result in a reduction in the number of hours for which the system can be operated due to low energy generation at lower irradiation conditions. Conversely, if longer operating hours are a requirement, a larger capital investment in solar modules or batteries would be required to allow the operation at times of lower solar irradiation. Other potential applications for PV module cooling include pumping bore water in remote locations, for which the slight increase in water temperature may not be a significant issue.

In general, forced convective cooling is more likely to be beneficial under conditions of high solar irradiation (>900 W m^{-2}) and high ambient temperature (>35 °C), such as those experienced in the summer in dry arid regions similar to northwest Mexico. In those regions, it is very likely that cooling will be beneficial for most of the summer daylight hours. However, in the spring and autumn, the times of the day for which cooling is beneficial are reduced, and cooling is basically of negligible use in the winter. As the weather conditions vary significantly with geographic location, a more detailed techno-economic case study that considers expected weather patterns is recommended in order to determine whether this strategy would be economically beneficial for a particular location.

5. Patents

The design of the heat exchanger system used to cool the photovoltaic panel using RO feed water, for the purpose of water desalination, has been filed as a patent application to the Mexican Institute of Intellectual Property (IMPI). This application for intellectual property protection, in the industrial design modality, was received by the local IMPI office on December 19, 2019 and is currently pending assessment.

Author Contributions: Conceptualization, M.F.S.V. and G.A.F.W.; methodology, G.A.F.W. and I.M.S.-T.; software, F.S.S.; validation, M.M.A.-O., G.A.F.W., and I.M.S.-T.; formal analysis, M.F.S.V. and M.M.A.-O.; investigation, M.F.S.V.; resources, G.A.F.W. and I.M.S.-T.; data curation, M.F.S.V.; writing—original draft preparation, M.F.S.V. and F.S.S.; writing—review and editing, all authors; visualization, all authors; supervision, G.A.F.W. and I.M.S.-T.; project administration, G.A.F.W.; funding acquisition, G.A.F.W., I.M.S.-T., and M.M.A.-O. All authors have read and agreed to the published version of the manuscript.

Funding: This research was funded by CONACYT, grant number PDCPN 2015-1221 and Cátedras Project 2338 and by the Instituto Tecnológico de Sonora through PROFAPI-2019-0068.

Institutional Review Board Statement: Not applicable.

Informed Consent Statement: Not applicable.

Data Availability Statement: The data presented in this study are available in this article.

Acknowledgments: The authors would like to acknowledge funding provided by CONACYT, grant number PDCPN 2015-1221, the Cátedras CONACYT Program (Project 2338), for the support of the PhD scholarship of student number (CVU:651531/Becario:626178/No.Apoyo:473376). We would also like to thank ITSON's Programa de Fomento y Apoyo a Proyectos de Investigación (PROFAPI-2019-0068) for funding provided for this study.

Conflicts of Interest: The authors declare no conflict of interest.

Abbreviations

Variables	Description	Units
A_m	Membrane area	m^2
A_{PV}	Active area of PVT module	m^2
A_{pa}	Area of the PVT module in contact with the air	m^2
A_{px}	Contact area of PVT module with cooling water	m^2
C_{pw}	Heat capacity of cooling water	$J\ kg^{-1}\ K^{-1}$
D	Solute diffusivity	$m^2\ s^{-1}$
d_h	Hydraulic diameter	m
E_e	Useful electrical energy produced over one day	W h
E_{PV}	Rate of energy input to the PVT module	W
E_w	Rate of energy input to the cooling water	W
f	Fanning friction factor	-
FF	Fill factor	-
f_θ	Angular dependence of solar absorptance	-
G_{beam}	Beam solar irradiation	$W\ m^{-2}$
G_{dif}	Diffuse solar irradiation	$W\ m^{-2}$
G_s	Total solar irradiation	$W\ m^{-2}$
h_a	Wind heat transfer coefficient	$W\ m^{-2}\ K^{-1}$
h_{ch}	RO membrane feed channel height	m
H_o	Extraterrestrial radiation on a horizontal surface	$W\ m^{-2}$
H_R	Relative humidity	%
$\Delta H_{p,tm}$	Transmembrane pressure-enthalpy change	$J\ kg^{-1}$
$\Delta H_{T,tm}$	Transmembrane temperature-enthalpy change	$J\ kg^{-1}$
$\Delta H_{s,r}$	Specific enthalpy change of solution for NaCl at reference conditions	$J\ kg^{-1}$
I_{sc}	Short-circuit current	A
J_v	Local volumetric permeate flux	$m\ s^{-1}$
k_{mt}	Mass transfer coefficient on the membrane surface	$m\ s^{-1}$
k_t	Hourly clearness index	-
L	RO module length	m
M_s	Molar mass of NaCl	$kg\ mol^{-1}$
P_e	Electric power available for the high-presure pump	W
P_{eo}	Electric power output from the PVT module	W
P_{LP}	Electric power required by the low-pressure pump	W
p	Pressure	Pa
p_b	Pressure along feed channel fluid in RO module	Pa
p_p	Permeate pressure	Pa
Δp_{PVT}	Pressure drop across the PVT heat exchanger	Pa
Δp_{tm}	Transmembrane pressure difference	Pa
Pr	Prandtl number	-
Q_b	Volumetric flow rate in the feed channel of the RO module	$m^3\ s^{-1}$
Q_p	Volumetric flow rate of RO permeate	$m^3\ s^{-1}$, $L\ min^{-1}$
Q_w	Cooling water volumetric flow rate	$m^3\ s^{-1}$, $L\ min^{-1}$
q_a	Rate of heat removal from the PVT module by convective heat transfer with the wind	W

q_r	Rate of heat removal from the PVT module radiative heat transfer with the sky	W
q_s	Rate of solar energy absorption by the PVT module	W
q_w	Rate of heat removal from the PVT module by forced convection with cooling water	W
q_x	Heat exchanged between PVT module and cooling water	W
R_g	Universal gas constant	J mol^{-1} K^{-1}
R_{int}	RO membrane intrinsic salt rejection	-
R_m	Hydraulic resistance of RO membrane	m^{-1}
R_{obs}	Observed salt rejection for RO membrane module	-
Re	Reynolds number	-
Sc	Schmidt number	-
Sh	Sherwood number	-
T	Temperature	°C, K
T_a	Ambient temperature	°C, K
T_b	Temperature along feed channel in RO module	°C, K
T_{dp}	Dew point temperature	°C
T_{PV}	PV module temperature	°C, K
$T_{PV,max}$	Maximum PV module temperature	°C
T_r	Reference temperature	°C
T_{sky}	Sky temperature	K
T_{wi}	Temperature of cooling water at PVT module inlet	°C
T_{wo}	Temperature of cooling water at PVT module outlet	°C
ΔT_{lm}	Logarithmic mean temperature difference between PV module and cooling water	K
U	Overall heat transfer coefficient for cooling water heat exchange	W m^{-2} K
u_b	Bulk feed flow velocity in membrane module	m s^{-1}
V	Voltage	V
v_a	Wind speed	m s^{-1}
V_{oc}	Open-circuit voltage	V
Vol_p	Permeate volume produced over one day	m^3
W	Power	W
w_b	Salinity mass fraction along feed channel fluid in RO module	-
w_p	Salinity mass fraction of RO permeate	-
Greek Symbols	Description	Units
α	PV module solar absorptivity	-
β	Angle of incidence between the solar beam irradiation and the horizontal plane	°
	Concentration polarisation modulus	-
ε	PV module emissivity	-
ϵ	Void fraction in feed channel of RO module	-
$\Delta\eta$	Efficiency drop of PVT module	%
η	Electrical efficiency of PVT module	%
η_c	Electrical efficiency of PVT module under forced convective cooling	%
η_{LP}	Energy efficiency of the low-pressure pump	%
η_u	Electrical efficiency of PV module at uniform temperature	%
φ	Osmotic coefficient	-
µ	Fluid viscosity	Pa s
π_m	Osmotic pressure on the feed side of the RO membrane surface	Pa
π_p	Osmotic pressure on the permeate side of the RO membrane surface	Pa
θ	Angle of incidence between the solar beam irradiation and the PV module	°
ρ	Density	kg m^{-3}
ρ_p	Density of the RO permeate	kg m^{-3}
ρ_w	Density of water	kg m^{-3}
σ	Stefan-Boltzmann constant	W m^{-2} K^{-4}
σ_T	Standard deviation of the PV module temperature distribution	K
A	Oscilloscope current sensing probe	
C	Capacitor	
HP	High-pressure	
LP	Low-pressure	
ODE	Ordinary differential equation	

PV	Photovoltaic
PVC	Polyvinyl chloride
PVT	Photovoltaic-thermal
R	Resistor
RO	Reverse osmosis
SW_1	Load capacitor switch 1
SW_2	Load resistor switch 2
V	Oscilloscope voltage sensing probe

Appendix A

This section presents thermographic images for each of the heat exchange configurations tested in this work, as well as schematic depiction of the expected flow lines. These are presented in Figure A1 for group B, in Figure A2 for group S, and in Figure A3 for group L. The images show areas with temperatures ranging from 25 to 69 °C. However, a scale with a temperature range of 30 to 45 °C is used to better visualise this range with a wider colour scale.

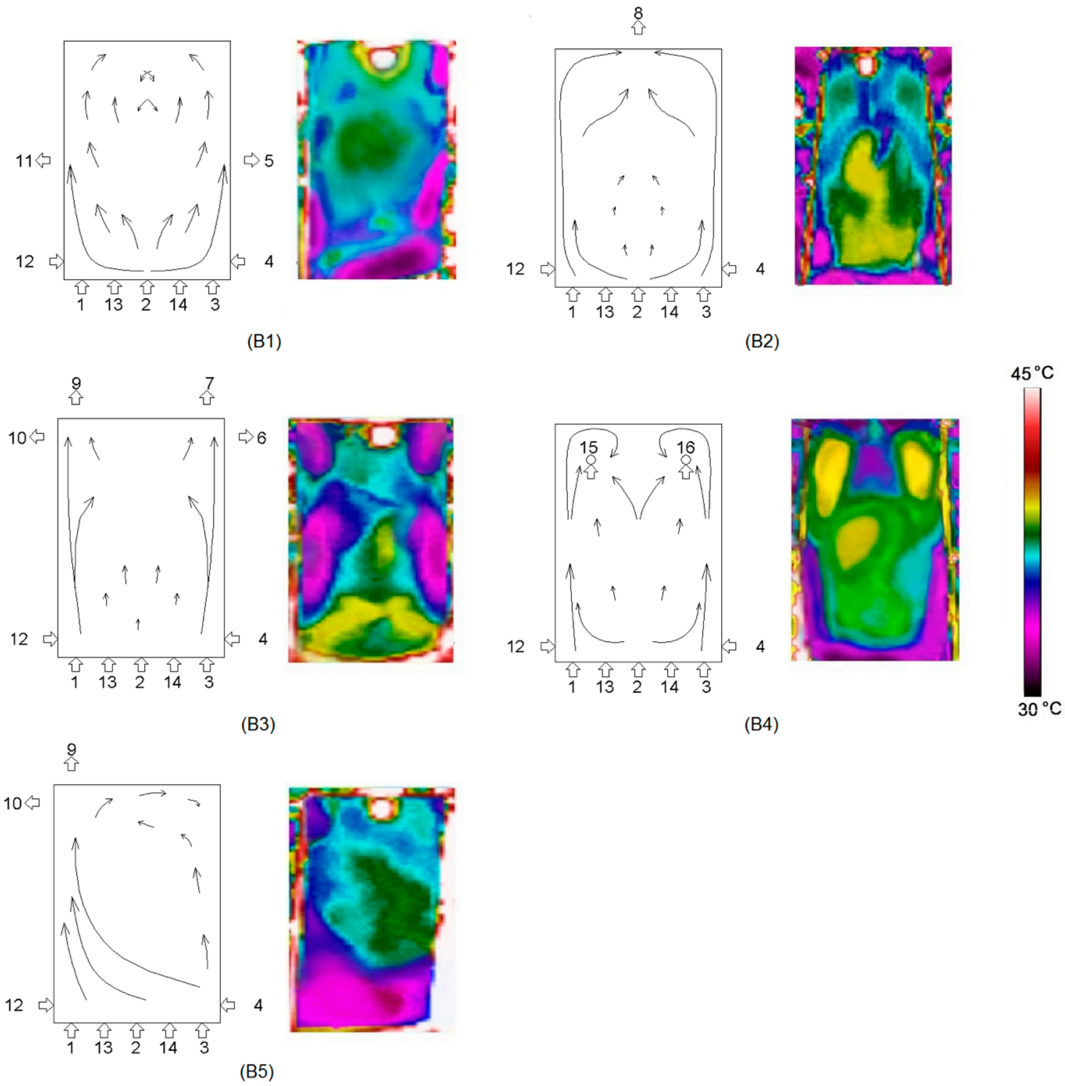

Figure A1. Diagrams of expected flow lines for group B configurations, alongside their respective thermographic images. The reader is referred to Table 2 for the description of each configuration.

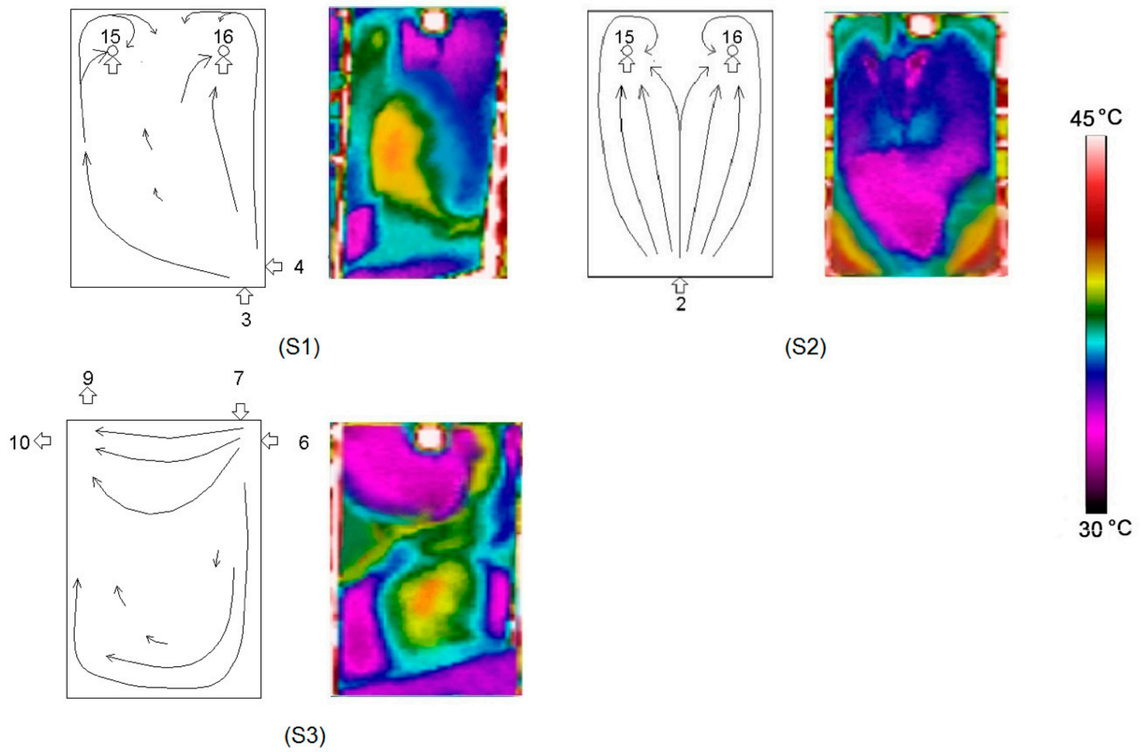

Figure A2. Diagrams of expected flow lines for group S configurations, alongside their respective thermographic images. The reader is referred to Table 2 for the description of each configuration.

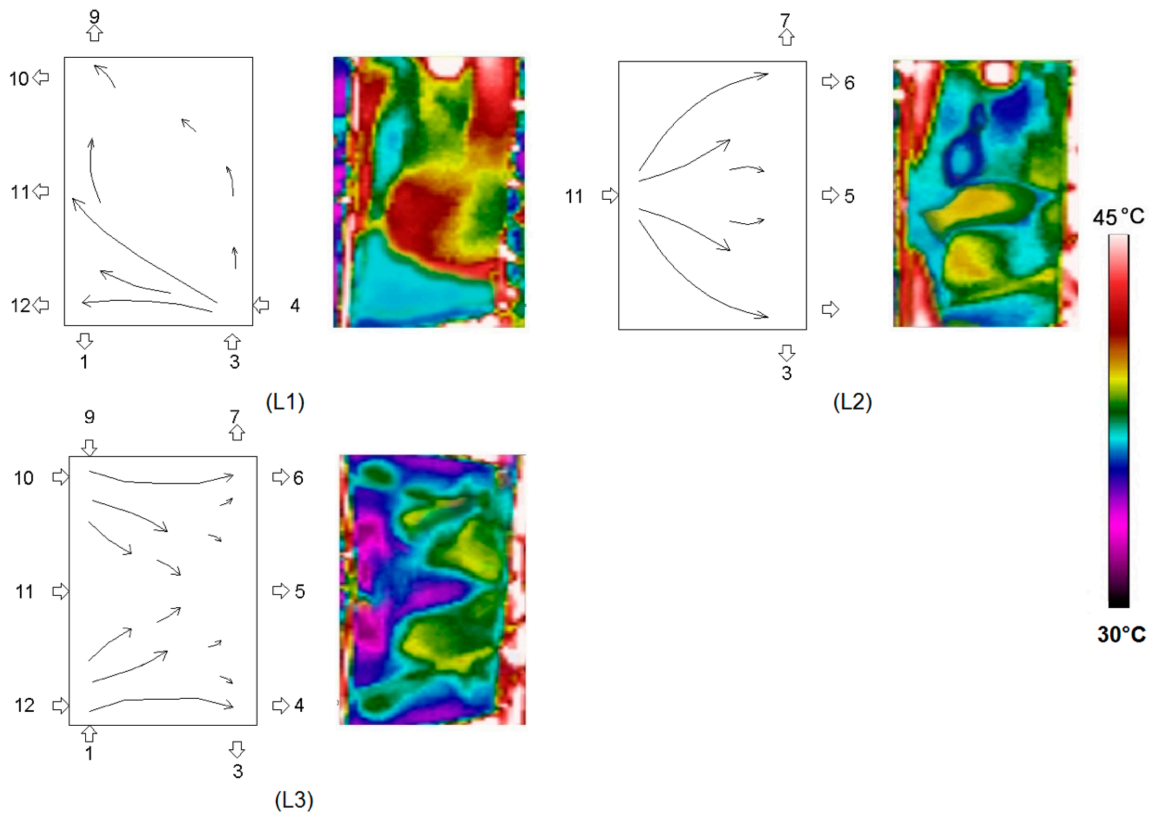

Figure A3. Diagrams of expected flow lines for group L configurations, alongside their respective thermographic images. The reader is referred to Table 2 for the description of each configuration.

Appendix B

This section presents the characteristic curve of the low-pressure (LP) pump used in the experiments for circulating feed water through the different heat exchange configurations tested in this paper. The curve presented in Figure A4 is used to determine the pressure drop across the PVT module and to determine the pumping energy requirements for a fit-for-purpose pump in the simulated PVT-RO system.

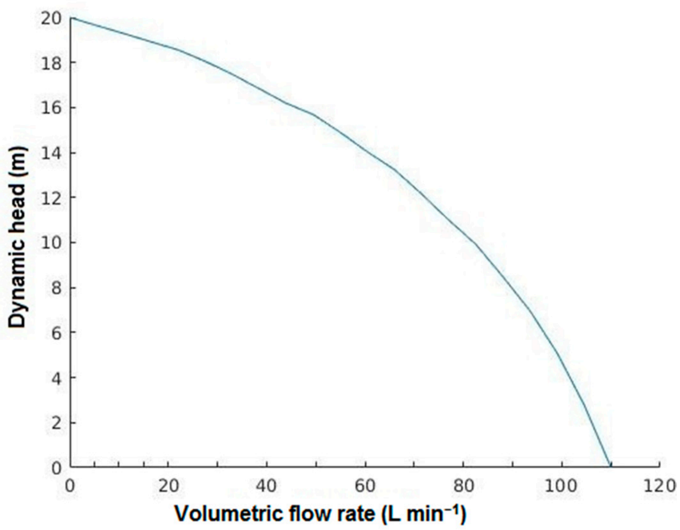

Figure A4. Experimental low-pressure pump characteristic curve.

The pressure drop in the PVT heat exchanger (Δp_{PVT}) is taken to be equal to the dynamic head supplied to the fluid by the experimental LP pump, multiplied by the gravitational acceleration and the density of the cooling water (ρ_w). Because the volumetric flow rate through the experimental LP pump is not easily controlled, the volumetric flow rate of cooling water through the PVT module (Q_w) was manipulated using a bypass valve after the LP pump outlet, with the bypass flow returning to the feed tank. Therefore, the total flow rate through the experimental LP pump (i.e., the sum of Q_w and the bypass flow) is used to determine the dynamic head from Figure A4, and this value is used to estimate Δp_{PVT}. This approach is followed for all the cooling configurations tested in this work.

Appendix C

This section presents and summarises the auxiliary equations required for the PVT-RO modelling described in Section 2.4.

The mathematical model for the high-pressure (HP) pump calculates the voltage and maximum output pressure, for a given volumetric flow rate operating condition and the electrical power available from the solar PVT module. This calculation is based on the technical datasheet of a HP DC pump (SunPumps SIJ 3.1-1500P-225 BL) which is capable of operating under the conditions necessary for brackish water RO. The technical data for the pump are fitted to a multilinear model of the form:

$$\begin{bmatrix} p \\ V_{pump} \end{bmatrix} = \begin{bmatrix} a_{0,1} & a_{1,1} & a_{2,1} & a_{3,1} & a_{4,1} & a_{5,1} \\ a_{0,2} & a_{1,2} & a_{2,2} & a_{3,2} & a_{4,2} & a_{5,2} \end{bmatrix} \begin{bmatrix} 1 \\ Q_w \\ Q_w^2 \\ P_e \\ P_e^2 \\ Q_w P_e \end{bmatrix} \tag{A1}$$

where p is the fluid outlet pressure in psi, V_{pump} is the voltage required by the pump in V, Q_w is the volumetric flow rate L min^{-1}, and P_e and is the electrical power available in W. The values of the coefficients for this multilinear fit are given in Table A1.

Table A1. Coefficient values for the multilinear regression in Equation (A1).

Coefficient	Value
$a_{0,1}$	−301.03
$a_{1,1}$	35.872
$a_{2,1}$	−2.6886
$a_{3,1}$	1.4446
$a_{4,1}$	-1.75×10^{-5}
$a_{5,1}$	-6.5214×10^{-2}
$a_{0,2}$	105.90
$a_{1,2}$	−6.6648
$a_{2,2}$	1.2169
$a_{3,2}$	1.2325×10^{-2}
$a_{4,2}$	1.24×10^{-7}
$a_{5,2}$	-1.1288×10^{-4}

The logarithmic mean temperature difference between the PV module and the cooling water (ΔT_{lm}) used in Equations (3) and (4) is given by:

$$\Delta T_{lm} = \frac{T_{wo} - T_{wi}}{\ln\left(\frac{T_{PV}-T_{wi}}{T_{PV}-T_{wo}}\right)} \tag{A2}$$

For the experiments described in Section 2.3, solar irradiation (G_s) data are obtained from pyranometer measurements. However, the pyranometer measures the solar radiation on a horizontal plane. Therefore, assuming that the angle of incidence between the solar beam irradiation (G_{beam}) and the horizontal plane is β, the following holds:

$$G_{beam} = \frac{G_s - G_{dif}}{\cos\beta} \tag{A3}$$

Diffuse irradiation (G_{dif}) in Equations (7) and (A3) is estimated as proposed by Boland et al. [35]:

$$G_{dif} = \frac{G_s}{1 + \exp(-5.03 + 8.6k_t)} \tag{A4}$$

where k_t is the hourly clearness index, defined in terms of the extraterrestrial radiation on a horizontal surface (H_0):

$$k_t = \frac{G_s}{H_0} \tag{A5}$$

The value of H_0 depends on the month of the year in question [27,36]. The angular dependence of solar absorptance (f_θ) in Equation (7) is given by [27]:

$$\begin{aligned} f_\theta = {} & 1 - 1.59 \times 10^{-3}\theta + 2.73 \times 10^{-4}\theta^2 - 2.3 \times 10^{-5}\theta^3 + 9.02 \times 10^{-7}\theta^4 \\ & -1.8 \times 10^{-8}\theta^5 + 1.77 \times 10^{-10}\theta^6 + 6.99 \times 10^{-13}\theta^7 \end{aligned} \tag{A6}$$

where θ is the incidence angle between the solar PV module and the solar beam irradiation, in degrees.

The wind heat transfer coefficient (h_a) in Equation (8) is given by [27]:

$$h_a = 5.7 + 3.8v_a \tag{A7}$$

where h_a is given in W m^{-2} K^{-1}, and v_a in m s^{-1}.

The sky temperature (T_{sky}) in Equation (9) is given by [27]:

$$T_{sky} = T_a \left\{ 0.71 + 0.0056 T_{dp} + 7.3 \times 10^{-5} T_{dp}^2 + 0.013 \cos \left[\frac{15\pi(t-12)}{180} \right] \right\}^{1/4} \tag{A8}$$

where T_{sky} and T_a are in K, T_{dp} is the dew point temperature in °C, and t is the time of the day in hours since midnight.

The dew point temperature (T_{dp}) in Equation (A8) can be obtained using Antoine equation parameters for the vapour pressure of water, such that:

$$T_{dp} = \left[\frac{1}{T_a + C} - \frac{\log_{10} R_H - 2}{B} \right]^{-1} - C \tag{A9}$$

where T_{dp} and T_a are in °C, R_H is given as a percentage, and the coefficient values for water vapour are B = 1730.63 and C = 233.426 [37].

The mass transfer coefficient in Equation (17) depends on the geometry and flow conditions inside the membrane module, and can be obtained from empirical equations that correlate the Reynolds (Re) and Schmidt (Sc) numbers to the Sherwood number (Sh). Schock and Miquel [33] give the following correlation for typical RO spacer-filled (FilmTec) spiral wound membrane module:

$$Sh = 0.065 Re^{0.875} Sc^{0.25} \tag{A10}$$

where the dimensionless numbers are defined as:

$$Re = \frac{\rho u_b d_h}{\epsilon \mu} \tag{A11}$$

$$Sc = \frac{\mu}{\rho D} \tag{A12}$$

$$Sh = \frac{k_{mt} d_h}{D} \tag{A13}$$

where D is the solute diffusivity. The bulk fluid velocity in the feed channel of the RO module is defined as:

$$u_b = \frac{Q_b L}{h_{ch} A_m} \tag{A14}$$

where A_m is the membrane area and L is the RO module length.

The membrane resistance (R_m) in Equation (15) is slightly temperature dependent and can be determined from DI water permeation data by varying the feed pressure, a process that is widely reported in the literature [38–40]. This process is repeated for several temperature values, and R_m is then fitted to a linear dependency on temperature based on experimental data:

$$R_m = 3.9598 \times 10^{14} - 1.0976 \times 10^{12} T_b \tag{A15}$$

where T_b is given in K, and R_m is given in m^{-1}. This fit was obtained experimentally for the particular membrane modelled, which in the case of this paper is a BW30 (DuPont) TFC RO membrane.

Salt passage through the membrane is modelled using the membrane intrinsic rejection, defined in terms of the salinity mass fraction on either side of the membrane, that is:

$$R_{int} = \frac{w_m - w_p}{w_m} \tag{A16}$$

On the other hand, the observed rejection (R_{obs}) in Equations (19) and (20) is defined in terms of the bulk and permeate salinity mass fractions, that is:

$$R_{obs} = \frac{w_b - w_p}{w_b} \tag{A17}$$

These two rejection definitions are related through the concentration polarisation modulus:

$$\Gamma = \left(\frac{1 - R_{obs}}{R_{obs}}\right)\left(\frac{R_{int}}{1 - R_{int}}\right) \tag{A18}$$

Similarly to membrane resistance, intrinsic rejection is also slightly temperature dependent. This relationship is determined experimentally for several temperature and salinity values, and R_{int} is then fitted to a linear dependency on temperature based on the experimental data:

$$R_{int} = 0.99976 - 1.487 \times 10^{-4} T_b \tag{A19}$$

where T_b is given in °C.

Appendix D

This section presents the weather data sets used for the prediction of permeate water production for the proposed PVT-RO system, as well as the resulting simulated average PVT outlet water temperatures. The input data were sourced from a local weather station in Ciudad Obregon, Mexico (27°29′35.2″ N 109°58′10.7″ W). These data are presented in Table A2 for summer conditions (24 July 2018), in Table A3 for autumn conditions (20 October 2019), and in Table A4 for winter conditions (3 January 2020).

Table A2. Weather data set for the summer day (24 July 2018) used in the PVT-RO simulations.

Time of Day (h)	G_s (W m^{-2})	H_R (%)	T_a (°C)	v_a (m s^{-1})
6–7	316.66	57.07	31.71	1.491
7–8	528.33	47.81	33.65	1.574
8–9	715.00	41.85	35.11	1.542
9–10	853.33	35.33	36.74	1.238
10–11	936.66	38.37	37.11	1.395
11–12	973.33	37.52	37.43	1.283
12–13	936.66	29.94	38.53	1.059
13–14	836.66	27.36	38.97	1.113
14–15	686.66	26.47	39.48	0.959
15–16	495.00	30.79	38.96	0.995
16–17	275.00	38.06	37.16	1.112

Table A3. Weather data set for the autumn day (20 October 2019) used in the PVT-RO simulations.

Time of Day (h)	G_s (W m^{-2})	H_R (%)	T_a (°C)	v_a (m s^{-1})
6–7	4.83	82.11	21.50	0.000
7–8	132.16	79.26	22.47	0.041
8–9	358.33	66.87	24.99	0.403
9–10	553.33	56.10	27.07	0.973
10–11	702.66	48.40	28.90	1.120
11–12	785.00	39.29	31.04	0.809
12–13	805.66	35.10	32.11	1.118
13–14	756.33	33.17	32.60	0.871
14–15	646.50	30.58	33.55	0.908
15–16	473.83	30.54	33.44	1.286
16–17	226.00	36.00	32.31	1.540
17–18	22.83	41.08	30.17	1.508

Table A4. Weather data set for the winter day (3 January 2020) used in the PVT-RO simulations.

Time of Day (h)	G_s (W m^{-2})	H_R (%)	T_a (°C)	v_a (m s^{-1})
6–7	0.00	87.66	10.04	0.000
7–8	9.50	88.05	9.87	0.000
8–9	143.00	87.51	10.75	0.211
9–10	373.00	78.96	13.24	1.517
10–11	534.16	65.64	16.16	1.259
11–12	644.00	51.78	18.58	1.302
12–13	685.66	41.61	20.65	1.363
13–14	660.16	32.71	21.76	1.246
14–15	569.00	26.25	22.57	1.246
15–16	412.33	24.67	23.19	1.042
16–17	186.66	24.42	22.91	1.193
17–18	11.00	38.23	20.59	0.869

Table A5 shows the effect of the PVT module configuration on the temperature of the cooling water exiting the module. The inlet water temperatures are 28.7 °C and 20 °C on 24 July 2018 and 20 October 2019, respectively. The water temperatures for 3 January 2020 are not included as implementing cooling on that day did not result in increased permeate production for the PVT-RO system.

Table A5. Average outlet water temperatures by PVT module configuration and cooling water volumetric flow rate.

Configuration	Cooling Water Flow Rate, Q_w (L min^{-1})			
	1	2	1	2
	PVT Average Outlet Water Temperature, T_{wo} (°C)			
	24 July 2018		20 October 2019	
B1	35.8 ± 2.7	32.1 ± 1.3	26.3 ± 2.4	22.6 ± 1.4
B2	32.9 ± 1.6	30.6 ± 0.7	23.3 ± 1.7	21.5 ± 0.8
B3	33.8 ± 2.0	31.6 ± 1.1	24.0 ± 2.1	22.3 ± 1.2
B4	32.1 ± 1.3	31.3 ± 1.0	22.7 ± 1.4	22.1 ± 1.1
B5	33.0 ± 1.7	31.1 ± 0.9	23.4 ± 1.8	21.9 ± 1.0
S1	32.8 ± 1.6	31.1 ± 0.9	23.3 ± 1.7	21.9 ± 1.0
S2	34.1 ± 2.1	31.7 ± 1.1	24.2 ± 2.2	22.3 ± 1.2
S3	32.3 ± 1.4	31.4 ± 1.1	22.9 ± 1.5	22.2 ± 1.4
L1	34.5 ± 2.2	32.3 ± 1.4	24.6 ± 2.3	22.8 ± 1.4
L2	32.8 ± 1.6	31.6 ± 1.1	23.3 ± 1.7	22.3 ± 1.2
L3	32.3 ± 1.4	31.1 ± 0.9	22.9 ± 1.5	21.9 ± 1.0

References

1. Pandey, V.P.; Shrestha, S. Evolution of the nexus as a policy and development discourse. *Water-Energy-Food Nexus Princ. Pract.* **2017**, *1*, 11–20. [CrossRef]
2. Cairns, R.; Krzywoszynska, A. Anatomy of a buzzword: The emergence of 'the water-energy-food nexus' in UK natural resource debates. *Environ. Sci. Policy* **2016**, *64*, 164–170. [CrossRef]
3. Armendáriz-Ontiveros, M.M.; Álvarez-Sánchez, J.; Dévora-Isiordia, G.E.; García, A.; Fimbres Weihs, G.A. Effect of seawater variability on endemic bacterial biofouling of a reverse osmosis membrane coated with iron nanoparticles (FeNPs). *Chem. Eng. Sci.* **2020**, *223*, 115753. [CrossRef]
4. Cherif, H.; Belhadj, J. Environmental Life Cycle Analysis of Water Desalination Processes. In *Sustainable Desalination Handbook*; Elsevier: Amsterdam, The Netherlands, 2018; pp. 527–559. [CrossRef]
5. Leijon, J.; Salar, D.; Engström, J.; Leijon, M.; Boström, C. Variable renewable energy sources for powering reverse osmosis desalination, with a case study of wave powered desalination for Kilifi, Kenya. *Desalination* **2020**, *494*, 114669. [CrossRef]
6. Khan, M.A.M.; Rehman, S.; Al-Sulaiman, F.A. A hybrid renewable energy system as a potential energy source for water desalination using reverse osmosis: A review. *Renew. Sustain. Energy Rev.* **2018**, *97*, 456–477. [CrossRef]

7. Eltawil, M.A.; Zhengming, Z.; Yuan, L. A review of renewable energy technologies integrated with desalination systems. *Renew. Sustain. Energy Rev.* **2009**, *13*, 2245–2262. [CrossRef]
8. Rezk, H.; Sayed, E.T.; Al-Dhaifallah, M.; Obaid, M.; El-Sayed, A.H.M.; Abdelkareem, M.A.; Olabi, A.G. Fuel cell as an effective energy storage in reverse osmosis desalination plant powered by photovoltaic system. *Energy* **2019**, *175*, 423–433. [CrossRef]
9. Elmaadawy, K.; Kotb, K.M.; Elkadeem, M.R.; Sharshir, S.W.; Dán, A.; Moawad, A.; Liu, B. Optimal sizing and techno-enviro-economic feasibility assessment of large-scale reverse osmosis desalination powered with hybrid renewable energy sources. *Energy Convers. Manag.* **2020**, *224*, 113377. [CrossRef]
10. Mostafaeipour, A.; Qolipour, M.; Rezaei, M.; Babaee-Tirkolaee, E. Investigation of off-grid photovoltaic systems for a reverse osmosis desalination system: A case study. *Desalination* **2019**, *454*, 91–103. [CrossRef]
11. Schies, A.; Went, J.; Heidtmann, C.; Eisele, M.; Kroemke, F.; Schmoch, H.; Vetter, M. Operating control strategies and dimensioning of photovoltaic powered reverse osmosis desalination plants without batteries. *Desalination Water Treat.* **2010**, *21*, 131–137. [CrossRef]
12. Raval, H.D.; Maiti, S. Ultra-low energy reverse osmosis with thermal energy recovery from photovoltaic panel cooling and TFC RO membrane modification. *Desalination Water Treat.* **2016**, *57*, 4303–4312. [CrossRef]
13. Siecker, J.; Kusakana, K.; Numbi, B. A review of solar photovoltaic systems cooling technologies. *Renew. Sustain. Energy Rev.* **2017**, *79*, 192–203. [CrossRef]
14. Luque, A.; Sala, G.; Arboiro, J. Electric and thermal model for non-uniformly illuminated concentration cells. *Sol. Energy Mater. Sol. Cells* **1998**, *51*, 269–290. [CrossRef]
15. Royne, A.; Dey, C.J.; Mills, D.R. Cooling of photovoltaic cells under concentrated illumination: A critical review. *Sol. Energy Mater. Sol. Cells* **2005**, *86*, 451–483. [CrossRef]
16. Bahaidarah, H.M.; Baloch, A.A.; Gandhidasan, P. Uniform cooling of photovoltaic panels: A review. *Renew. Sustain. Energy Rev.* **2016**, *57*, 1520–1544. [CrossRef]
17. Zhang, C.; Shen, C.; Wei, S.; Wang, Y.; Lv, G.; Sun, C. A review on recent development of cooling technologies for photovoltaic modules. *J. Therm. Sci.* **2020**, *29*, 1410–1430. [CrossRef]
18. Raval, H.D.; Maiti, S.; Mittal, A. Computational fluid dynamics analysis and experimental validation of improvement in overall energy efficiency of a solar photovoltaic panel by thermal energy recovery. *J. Renew. Sustain. Energy* **2014**, *6*, 033138. [CrossRef]
19. Jin, X.; Jawor, A.; Kim, S.; Hoek, E.M.V. Effects of feed water temperature on separation performance and organic fouling of brackish water RO membranes. *Desalination* **2009**, *239*, 346–359. [CrossRef]
20. Monjezi, A.A.; Chen, Y.; Vepa, R.; Kashyout, A.E.-H.B.; Hassan, G.; Fath, H.E.-B.; Kassem, A.E.-W.; Shaheed, M.H. Development of an off-grid solar energy powered reverse osmosis desalination system for continuous production of freshwater with integrated photovoltaic thermal (PVT) cooling. *Desalination* **2020**, *495*, 114679. [CrossRef]
21. Spertino, F.; Ahmad, J.; Ciocia, A.; Di Leo, P.; Murtaza, A.F.; Chiaberge, M. Capacitor charging method for I–V curve tracer and MPPT in photovoltaic systems. *Sol. Energy* **2015**, *119*, 461–473. [CrossRef]
22. Sharqawy, M.H.; Lienhard, J.H.; Zubair, S.M. Thermophysical properties of seawater: A review of existing correlations and data. *Desalination Water Treat.* **2010**, *16*, 354–380. [CrossRef]
23. Sun, H.; Feistel, R.; Koch, M.; Markoe, A. New equations for density, entropy, heat capacity, and potential temperature of a saline thermal fluid. *Deep Sea Res. Part I Oceanogr. Res. Pap.* **2008**, *55*, 1304–1310. [CrossRef]
24. Isdale, J.D.; Morris, R. Physical properties of sea water solutions: Density. *Desalination* **1972**, *10*, 329–339. [CrossRef]
25. Gosset, E. Another differences calculus based on standar desviation and confidence interval. *Stat. Ref.* **1917**, *26*, 66–72.
26. Kaiser, H.F. An index of factorial simplicity. *Psychometrika* **1974**, *39*, 31–36. [CrossRef]
27. Duffie, J.A.; Beckman, W.A. *Solar Engineering of Thermal Processes*, 4th ed.; Wiley: Hoboken, NJ, USA, 2013.
28. Toh, K.Y.; Liang, Y.Y.; Lau, W.J.; Fimbres Weihs, G.A. The techno-economic case for coupling advanced spacers to high-permeance RO membranes for desalination. *Desalination* **2020**, *491*, 114534. [CrossRef]
29. Bartholomew, T.V.; Mauter, M.S. Computational framework for modeling membrane processes without process and solution property simplifications. *J. Membr. Sci.* **2019**, *573*, 682–693. [CrossRef]
30. Chapra, S.C.; Canale, R.P. *Numerical Methods for Engineers*, 6th ed.; McGraw-Hill: New York, NY, USA, 2010; p. 968.
31. Kedem, O.; Katchalsky, A. Thermodynamic Analysis of the Permeability of Biological Membranes to Non-Electrolytes. *Biochim. Biophys. Acta* **1958**, *27*, 229. [CrossRef]
32. FILMTEC. FILMTEC 8″ Brackish Water RO Element Specifications. In *Product Information*; FilmTec Corporation, Ed.; FILMTEC: Minneapolis, MN, USA, 1988; Volume 609-00616-0808.
33. Schock, G.; Miquel, A. Mass transfer and pressure loss in spiral wound modules. *Desalination* **1987**, *64*, 339–352. [CrossRef]
34. Sivertsen, E.; Holt, T.; Thelin, W.R. Concentration and Temperature Effects on Water and Salt Permeabilities in Osmosis and Implications in Pressure-Retarded Osmosis. *Membranes* **2018**, *8*, 39. [CrossRef]
35. Boland, J.; Ridley, B.; Brown, B. Models of diffuse solar radiation. *Renew. Energy* **2008**, *33*, 575–584. [CrossRef]
36. Ridley, B.; Boland, J.; Lauret, P. Modelling of diffuse solar fraction with multiple predictors. *Renew. Energy* **2010**, *35*, 478–483. [CrossRef]
37. Reid, R.C.; Prausnitz, J.M.; Sherwood, T.K. *The Properties of Gases and Liquids*, 3rd ed.; McGraw-Hill: New York, NY, USA, 1997.
38. Chong, T.H.; Wong, F.S.; Fane, A.G. Enhanced concentration polarization by unstirred fouling layers in reverse osmosis: Detection by sodium chloride tracer response technique. *J. Membr. Sci.* **2007**, *287*, 198–210. [CrossRef]

39. Armendáriz-Ontiveros, M.M.; García García, A.; de los Santos Villalobos, S.; Fimbres Weihs, G.A. Biofouling performance of RO membranes coated with Iron NPs on graphene oxide. *Desalination* **2019**, *451*, 45–58. [CrossRef]
40. Liang, Y.Y.; Fimbres Weihs, G.A.; Wiley, D.E. Comparison of oscillating flow and slip velocity mass transfer enhancement in spacer-filled membrane channels: CFD analysis and validation. *J. Membr. Sci.* **2020**, *593*, 117433. [CrossRef]